

AD-A265 734



2

**Efficient Optical Logic, Interconnections and
Processing Using Quantum Confined Structures**

AFOSR #89-0549 - FINAL REPORT

4/31/93

by

L. A. Coldren: Principal Investigator

A.C. Gossard: Co-Principal Investigator

C.C. Barron and G. Thompson: Students

**M. Whitehead and Cathal Mahon: Visiting Research
Engineers**

ECE Technical Report #93-10

DTIC QUALITY INSPECTED 2

Accession For	
NTIS CRA&I	<input checked="" type="checkbox"/>
DTIC TAB	<input type="checkbox"/>
Unannounced	<input type="checkbox"/>
Justification	
By	
Distribution /	
Availability Codes	
Dist	Avail and/or Special
A-1	

DTIC
ELECTE
JUN 14 1993
S E D

DTIC QUALITY INSPECTED 2

Department of Electrical & Computer Engineering

University of California at Santa Barbara

May 20, 1993

TABLE OF CONTENTS

I.	INTRODUCTION	
1.	Summary of Work	1
2.	Goals and Figures of Merit for Transverse Electro-Optic Modulators	2
II.	SYMMETRIC (ELECTRO-REFRACTIVE) FABRY-PEROT MODULATORS (SFPMs)	
1.	Review of Operating Principles	7
2.	Performance of SFPMs	7
III.	ASYMMETRIC (ELECTROABSORPTIVE) FABRY-PEROT MODULATORS (AFPMs)	
1.	Principles of AFPM Device Operation	11
2.	Low Voltage, Low Insertion Loss, and High Contrast AFPM	12
3.	Comparison of Various FP Modulators	18
4.	Superlattice AFPM with a Normally-Off Characteristic	19
IV.	SENSITIVITY ANALYSIS	
1.	Wavelength, Voltage and Temperature Effects	22
2.	MBE Growth Tolerances	28
3.	Power Saturation Limitations	36
4.	Power Dissipation Considerations for Arrays	41
V.	HIGH FREQUENCY OPERATION OF FP MODULATORS	
1.	Device Structure, Fabrication and Measurement	46
2.	Design Methodology	57
VI.	CIRCUITS AND APPLICATIONS	
1.	Superlattice AFP Bistable SEED	61
2.	Superlattice AFP Linearized SEED	64
3.	Fiber to Fiber Coupling Interface for Transverse Modulators	66
VII.	Conference and Journal Publications	75
VIII.	Personnel	80



REPORT DOCUMENTATION PAGE			Form Approved OASD No. 0704-0188	
<small>Full reporting burden for this collection of information is estimated to average 1 hour per response, including the time for reviewing instructions, searching existing data sources, gathering and maintaining the data needed, and completing and reviewing the collection of information. Send comments regarding this burden estimate or any other aspect of this collection of information, including suggestions for reducing this burden, to Washington Headquarters Services, Directorate for Information Operations and Reports, 1215 Jefferson Davis Highway, Suite 1204, Arlington, VA 22202-4302, and to the Office of Management and Budget, Paperwork Reduction Project (0704-0188), Washington, DC 20503.</small>				
1. AGENCY USE ONLY (Leave blank)	2. REPORT DATE 31 Apr 93	3. REPORT TYPE AND DATES COVERED Final Report 30 Sep 89 - 31 Mar 93		
4. TITLE AND SUBTITLE Efficient Optical Logic, Interconnections and Processing Using Quantum Confined Structures		5. FUNDING NUMBERS AFOSR-89-0549		
6. AUTHOR(S) Professors L. Coldren, A Gossard C Barron, G Tompson, M Whitehead, C Mahon		AFOSR TR. 89-0549-5		
7. PERFORMING ORGANIZATION NAME(S) AND ADDRESS(ES) Department of Electrical & Computer Engineering University of California Santa Barbara CA 93106		8. PERFORMING ORGANIZATION REPORT NUMBER		
9. SPONSORING/MONITORING AGENCY NAME(S) AND ADDRESS(ES) AFOSR/NE 110 Duncan Avenue Suite B115 Bolling AFB DC 20332-0001		10. SPONSORING/MONITORING AGENCY REPORT NUMBER 2305/DS		
11. SUPPLEMENTARY NOTES				
12. DISTRIBUTION/AVAILABILITY STATEMENT UNLIMITED		13. DISTRIBUTION CODE		
14. ABSTRACT (Maximum 200 words) This is the final report of AFOSR-89-0549. It summarizes work extending over the entire contract period which began 30 Sept 1989. The work is not reported in chronological order. Rather, it is organized according to subject, and it is intended to be somewhat tutorial, although only work at UCSB is included. (SEE REPORT FOR MORE DETAIL)				
15. SUBJECT TERMS		16. NUMBER OF PAGES		
		17. PRICE CODE		
18. SECURITY CLASSIFICATION OF REPORT UNCLASSIFIED	19. SECURITY CLASSIFICATION OF THIS PAGE UNCLASSIFIED	20. SECURITY CLASSIFICATION OF ABSTRACT UNCLASSIFIED	21. LIMITATION OF ABSTRACT UNLIMITED	

I.1 Summary of Work

This is the final report for AFOSR-89-0549. It summarizes work extending over the entire contract period which began 30 September 1989. The work is not reported in chronological order. Rather, it is organized according to subject, and it is intended to be somewhat tutorial, although only work at UCSB is included.

The report begins by reviewing what aspects of transverse modulators are important for various applications. Certain 'figures-of-merit' are proposed. Electro-refractive and electro-absorptive modulators are then introduced. The electro-refractive type, which we first explored in a previous AFOSR program, has the desirable attribute of switching light between reflection and transmission, rather than absorbing it. Thus, these modulators tend to not saturate at high optical powers or have thermal dissipation problems. However, for reasonable modulation depth, a relatively high-finesse Fabry-Perot cavity is required. This can be a problem if a bandwidth of a nanometer (i.e., $\sim 0.1\%$ of the wavelength) or more is desired to accomodate some temperature range or nonuniformities in arrays. The electro-absorptive design uses an unbalanced, asymmetric Fabry-Perot cavity. By adding relatively low-loss levels with relatively low voltages across the cavity, the asymmetric cavity can be balanced, pulling the reflection down to zero. The reflection change as well as the contrast can be high for a given applied voltage. In this case the cavity finesse also tends to be lower than for the symmetric, refractive modulator case.

Most of the balance of the report focusses on the asymmetric Fabry-Perot design. An important consideration for these devices is the feasibility of reproducibly manufacturing them, and this is compounded by a desire to use them at reasonable powers in large arrays. Thus, we consider their sensitivity to various fabrication as well as environmental variations. Next, we explore the high-frequency modulation capabilities of these modulators. It is shown that very high bandwidth is possible. More than 20GHz has been demonstrated, and greater than 40GHz is predicted. Finally, some of the devices are evaluated in self-electrooptic effect circuit geometries. Excellent contrast and hysteresis is demonstrated.

1.2. Goals and Figures of Merit for Transverse Electro-Optic Modulators

Highly efficient electro-absorption and electro-refraction effects in semiconductor multiple quantum wells and superlattices, along with increased system demands have advanced high-performance optical modulators which can be used in various applications: as an intra-laser-cavity controlling device, transmitter of telecommunications including interconnections for integrated circuits, and optical information processing.

Among various design issues for practical applications, one of the important considerations is low drive power, e.g. low operating voltage swing in electro-optic modulators. This is important for compatibility with digital electronics. Waveguide (in-plane) devices tend to provide low drive voltages (≈ 1 volt) because the field is applied perpendicular to the light propagation direction [1]; however, the coupling of the light into the waveguide adds complexity to practical implementations. On the other hand, although coupling is relatively easy, surface-normal (transverse) devices have tended to require high drive voltages (> 10 volts) due to short interaction lengths [1]. The use of a Fabry-Perot cavity to provide optical feedback has recently reduced required drive voltages to as low as 2V, however.

A related device parameter to drive voltage is the normalized electro-optic transfer function (M_V) [2], defined as the percentage modulation of the input optical power per unit drive voltage. Early transverse modulators had M_V s of $\leq 8\%/V$, and efficient waveguide modulators have a representative value of $< 15\%/V$ [1]. Current figures for surface normal modulators are as high as $20\%/V$.

The contrast ratio, or the ratio of the power reflectivity in the on state to the power reflectivity in the off state is another important figure of merit for modulators. Ideally, a device has a power reflectivity in the on state of $R_{ON}=1$, and in the off state of $R_{OFF}=0$. In other words, a contrast ratio which is infinite. Achieving such a contrast ratio is possible with surface normal modulators. However, since an infinite contrast ratio can be achieved for any value of R_{ON} , provided that $R_{OFF}=0$, it is important to consider the insertion loss in conjunction with the contrast ratio. Low insertion loss is important because there will be system constraints on the signal power which must be transmitted

by the modulator for low BER. Devices with a nearly infinite contrast ratio and an insertion loss of only 1.65db have been produced.

It should be noted that we focus here on "single ended" operation. It has been suggested that differential operation may be appropriate, in which case $\Delta R = R_{On} - R_{Off}$ is the important parameter.

Drive voltage, contrast ratio, and insertion loss are the three fundamental device parameters which characterize modulators. However, when one considers use in a practical system, a number of other parameters become important.

Bit rate is an obvious consideration for any system. Therefore, the electrical bandwidth of modulators is an important consideration. The resistance in the contacts and the doped p and n regions, and the capacitance due to the undoped intrinsic region lead to an RC time constant which limits the device speed of operation. Device design and geometry may reduce this time constant to $<10\text{ps}$.

The range of optical power over which the modulator will operate is another important system consideration. There are two important effects at high optical power. First, the exciton can be saturated. Second, screening effects can reduce the field in the quantum wells at a given applied field, thereby reducing the effective modulation. The finite saturation velocity of the carriers and the intrinsic region thickness combine to give a second time constant limitation at high power.

A thick active region lowers the capacitance, but raises the transit time. Hence, there is a tradeoff in the design of modulators which must be made depending upon the specific application.

Optical bandwidth may be defined as the bandwidth over which the modulator maintains a certain contrast ratio, e.g. 10, or equivalently a maximum off state power reflectivity, e.g. $R_{Off}=5\%$. These are roughly equivalent due to the fact that R_{On} is very flat as a function of wavelength as compared to R_{Off} . The optical bandwidth is an important consideration because of possible variations in the wavelength of the laser source, and thereby variations in the wavelength of operation. In addition, if the modulator is of the absorption variety it can make an excellent wavelength selective detector.

If one considers large arrays of such modulators, issues such as power dissipation and uniformity become significant. Optical power absorbed and electrical power delivered both contribute to the total power which must be dissipated. Clearly, low voltage and low insertion loss are important factors in achieving low power dissipation. Uniformity is a general term referring to the capability of growing a uniform structure across an entire wafer.

A final factor which will impact the conditions under which the device will perform acceptably is temperature. Temperature causes the bandgap, and thereby the exciton, to change and also changes the index, and thereby the location of the Fabry-Perot modes. Whether or not external temperature control (e.g. TE cooler) is necessary is clearly dependent upon the sensitivity of the device parameters to temperature.

The first demonstration of transverse modulators by Wood et al. [1] in 1985 employed a simple PIN-MQW transmission configuration with the QCSE. Although more than 30% transmission has been obtained with only 8 volts, the contrast ratios are quite limited (≤ 3 dB).

Using the simple transmission configuration, the contrast ratio has been improved to ≈ 7 dB [3] by using a much thicker active region, but the required voltage increases and therefore M_V decreases. By incorporating a single reflector (monolithically grown quarter-wavelength stack, or deposited-metal) on one side of the active region and an anti-reflection layer on the other side, the effective interaction length is doubled from the simple transmission configuration [4,5]. Both the contrast and the transfer function are doubled for the same voltage swing.

M_V increases from 0.8 to 1.5 %/V due to the addition of the reflector. Using two reflectors to form a Fabry-Perot (FP) cavity [6,7], the interaction length can be increased even more, and the amount of enhancement depends on the finesse given by the mirror reflectivities [9]. Although the introduction of FP structures places a limit on the optical bandwidth, BW_O over which the device can be operated, the required voltage swing is greatly reduced. Therefore, as long as BW_O remains large enough, e.g., no less than the room temperature linewidth of quantum well heavy hole exciton absorption peak, the use of FP structures to improve the performance is justified.

Both electro-refraction [6,7] and electro-absorption [8] effects can be used with FP structures. To use the electro-refraction effect, the mirror reflectivities on both sides of the FP cavity are designed to be the same (index-tuned symmetric FP or SFP Δn), and the index change is used to tune the FP mode to achieve the modulation. Depending on the operating wavelength, the device can be normally-on (reflecting with no bias) or normally-off (reflecting with bias). As much as 4 %/V has been achieved with contrast ratios more than 15 dB [9]. However, due to relatively large finesse, BW₀ is quite limited ($\approx 5\text{\AA}$).

Although both electro-absorption and electro-refraction effects can be used with multiple quantum wells (MQWs), the electro-refraction effect should be used at a wavelength that is away from the sharp excitonic absorption edge, in order to avoid any induced absorption change and to lose the advantages of sharp excitonic features [10]. Since both effects are reduced with separation from the exciton, it is generally true that MQWs work more efficiently in the electro-absorption mode than in the electro-refraction mode; that is, FPs with an absorption change ($\Delta\alpha$) tend to operate with lower voltages than the SFP Δn , or for the same voltage, they have wider BW₀. However, SFP Δn devices switch the light instead of absorbing it, and such an operating mode can be quite useful for photonic switching and communication applications in which one wishes to preserve the optical energy.

Unequal mirrors are used with electro-absorption effects to implement asymmetric Fabry-Perot (AFP) modulators [10,11]. The modulation mechanism operates as follows. Without cavity loss, the overall reflectivity is quite high if the bottom mirror reflectivity is made close to unity and the top mirror reflectivity is somewhat less. With applied fields, the increased cavity loss reduces the effective reflectivity from the bottom mirror at the top surface, and the overall reflectivity can be made zero when the effective reflectivity from the bottom has an equal magnitude to the top mirror reflectivity, yielding the off state. The first experiments with AFPs simply used the semiconductor-air interface as the top mirror [8,11], and comparable M_V 's are obtained with significantly wider BW₀'s ($\geq 3\text{ nm}$) than for SFP Δn 's.

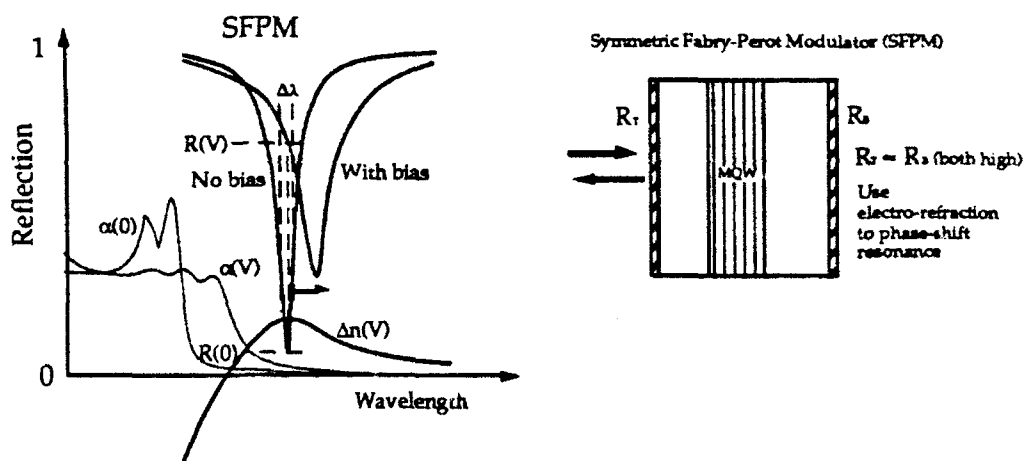
More importantly, when a $\approx 75\%$ reflectivity top mirror is used, a voltage swing as low as 2 volts is enough to change the device reflectivity by more than 40 %, i.e. $> 20\text{ \%}/V$ [12]. Such an M_V represents the-state-of-the-art in transverse modulator performance, and we

will discuss such a device family using asymmetric Fabry-Perot structures in more detail in this report.

II. Symmetric (Electrorefractive) Fabry-Perot Modulators (SFPMs)

II.1. Review of Operating Principles

The intent behind incorporating a Fabry-Perot étalon into a MQW electrooptic modulator is to increase the interaction length between the active material and the light beam, as compared to simple transmission or double-pass reflection designs [3–5]. Modulation is achieved by modifying the shape of a Fabry-Perot cavity resonance with an electric field. We began our work on Fabry-Perot modulators by concentrating on modulation of the refractive index in high-finesse structures, which phase shifts the cavity resonance. Low-finesse asymmetric FPMs have the advantage of increased optical bandwidth. For some applications, however, such as a four-port optical switch which requires the modulator to operate simultaneously in transmission and reflection, the symmetric version retains its appeal.



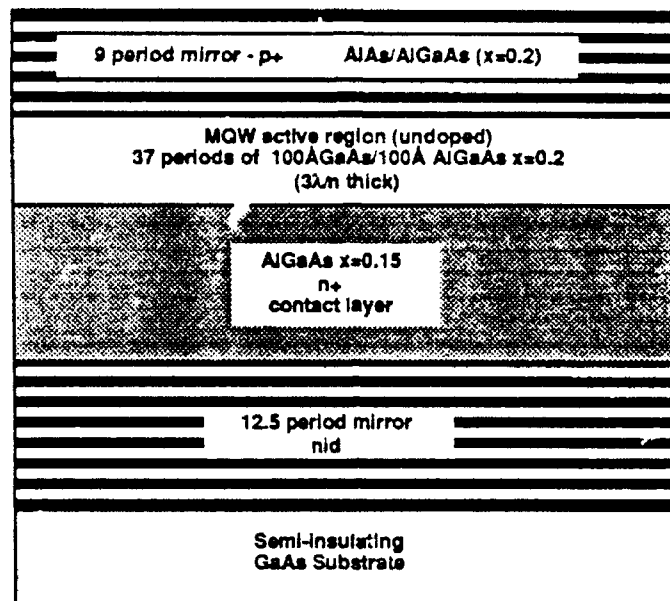
Efficient modulation in a high-finesse FP cavity by shifting the cavity resonance through electrorefraction.

Figure II.1

II.2. Performance of SFPMs

Prior to this contract we presented measurements of a symmetric MQW FP modulator with a contrast ratio of $\approx 10:1$ for drive voltages as low as 7 V. Since then, we have grown and characterized similar modulators with contrast ratios as high as 30:1 with an 8 V bias.[9] The device performance (contrast ratio, insertion loss, drive voltage) depends

largely on the placement of the FP resonance, which is determined by the exact cavity length. To illustrate the effect of resonance placement relative to the exciton wavelength, we present here measurements of two SFPMs fabricated from the same MBE-grown wafer. The device structure consists of a 9-period front mirror and a 12.5-period back mirror, with a nominally $0.75\ \mu\text{m}$ layer of MQW material (100\AA GaAs/ 100\AA $\text{Al}_{0.2}\text{Ga}_{0.8}\text{As}$). We intentionally refrained from rotating the wafer during growth of the active region in order to produce devices with a range of operating wavelengths. The structure is shown schematically below.



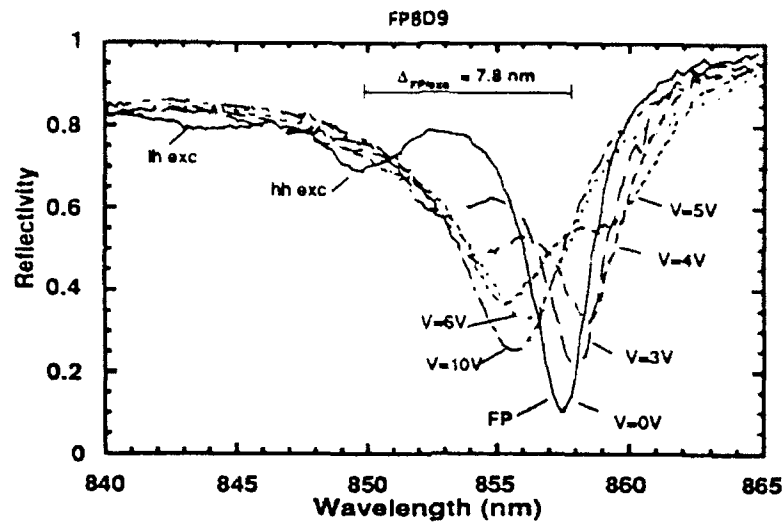
A schematic of the reduced voltage, improved contrast SFPM structure.

Figure II.2

The effect of operating with the FP resonance at two different wavelengths relative to the MQW absorption edge is illustrated in Figures II.3-II.6. Device "FP8D9", for example, has the operating wavelength at $\approx 857\text{nm}$ and $7.8\ \text{nm}$ separation between the FP resonance and the heavy hole exciton, while device "FP8E1" has its FP resonance at $\approx 878\text{nm}$ and a $\Delta_{\text{FP/exciton}}$ of 25nm .

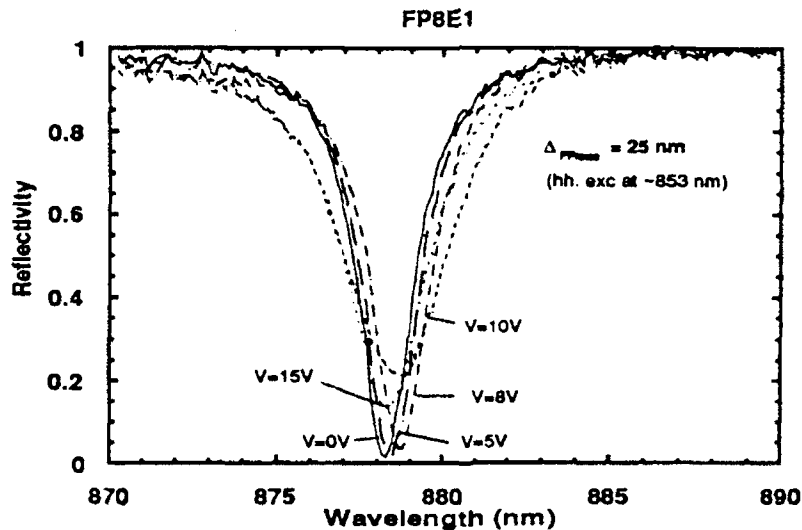
The data in Fig. II.5 show that a device such as "FP8D9" which operates relatively close to the absorption edge requires less bias to shift the FP resonance, and has lower insertion loss, but also has limited contrast because of its higher zero-field absorption. Operating

relatively far away from the absorption edge (device "FP8E1", Fig. II.6) increases the potential contrast but also increases the drive voltage and insertion loss.



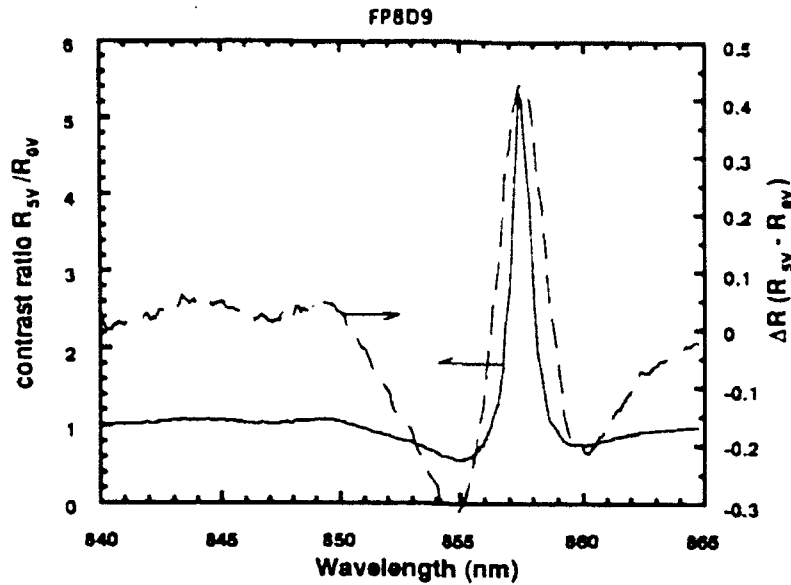
Measured reflection spectra for a FP structure with 9-period top mirror, 12.5-period mirror bottom mirror, and $3\lambda/n$ -thick MQW active medium. The wavelength separation between the FP resonance and the excitonic heavy-hole absorption, $\Delta_{FP/exc}$, is 7.8nm in this case.

Figure II.3



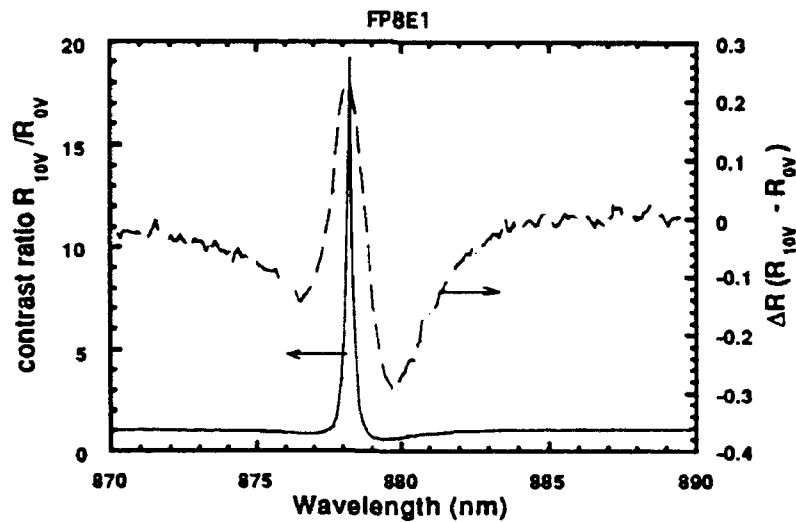
Measured reflection spectra for a FP structure with 9-period top mirror, 12.5-period mirror bottom mirror, and $3\lambda/n$ -thick MQW active medium. The wavelength separation between the FP resonance and the excitonic heavy-hole absorption, $\Delta_{FP/exc}$, is 25nm in this case.

Figure II.4



Contrast ratio and ΔR vs V for MQW-based active structure used for data of Fig. II.3. The bias is changed from 0V to 5V. The FP mode is quite close to the exciton absorption edge ($\Delta FP/exc = 9.9nm$), and there is some absorption at zero field, causing the reflection at the FP resonance to be non-zero; the contrast ratio is thus reduced. The FP mode shift at lower fields is accentuated and the voltage required for a high ΔR is reduced.

Figure II.5



Contrast ratio and ΔR vs V for MQW-based active structure used for data of Fig. II.4. The bias is changed from 0V to 10V. $\Delta FP/exc$ is higher for this sample; thus it takes more voltage to shift the resonance. The FP mode dips quite sharply to zero, making the contrast ratio high.

Figure II.6

III. Asymmetric (Electroabsorptive) Fabry-Perot Modulators (AFPMs)

III.1. Principles of AFPM Device Operation

A Fabry-Perot structure with MQW as the active material can either operate with electro-absorption or electro-refraction effects by designing the Fabry-Perot mode to locate closer to or further away from the excitons. The latter mode of operation has been described in detail in Ref. [9] where the mirrors on both sides of the cavity are made symmetric, i.e. equally reflective. To make use of the electro-absorption effect, the Fabry-Perot cavity can be symmetric or asymmetric. As will be discussed later in Section III.3, the asymmetric FP (AFP) structure [8,11] is found to be the more efficient structure for low voltage operation.

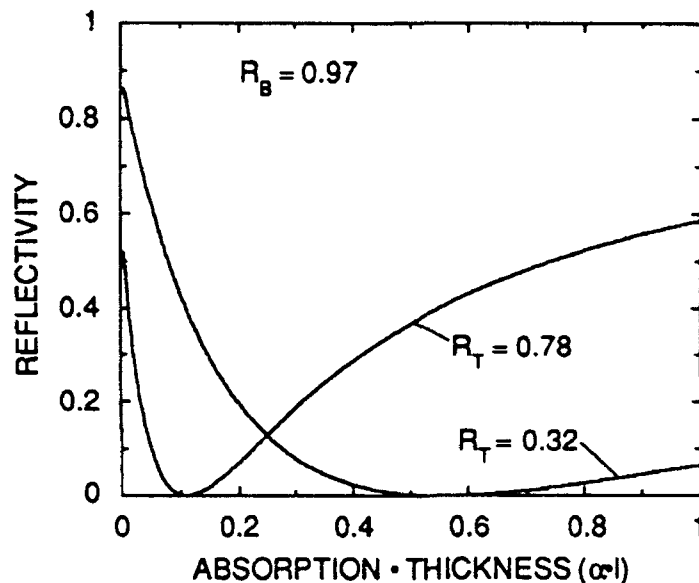
The top (bottom) mirror of an AFP structure has an amplitude reflection coefficient of $r_t(b)$ and power reflectivity of $R_T(B)=|r_t(b)|^2$, viewed from the cavity. $R_B > R_T$ is used in the design. Written in terms of the power reflectivities, the total power reflectivity from the Fabry-Perot is given by:

$$R_{FP} = \frac{|\sqrt{R_T} - \sqrt{R_B} \exp(-\alpha l)|^2}{|1 - \sqrt{R_T R_B} \exp(-\alpha l)|^2} \quad (1)$$

Assuming $R_B=0.97$, Figure III.1 plots R_{FP} as a function of $\alpha \cdot l$ for two different R_T 's. In the experiments described in the next section, we use a quarter wavelength stack of $Al_{0.2}Ga_{0.8}As$ and $AlAs$ as the top mirror, and the available mirror reflectivities are discrete from 0.32 to 0.78 as the number of periods increase from 0 to 5. As the loss in the cavity changes, the overall reflectivity of the Fabry-Perot structure is modulated. For example, when $\alpha \cdot l$ changes from 0.02 to 0.11, the reflectivity changes from 50 % (on) to 0 % (off) with $R_T=0.78$. This is the basic operating principle of AFP modulators. Depending on whether the absorption increases (e.g. QCSE) or decreases (Wannier-Stark localization) as the field increases, the device at zero bias can be either on (normally-on) or off (normally-off) [13]. The fact that

$$R_B \exp(-2\alpha l) = R_T \quad (2)$$

makes R_{FP} zero is the most interesting property of the AFP modulators. Conventional absorption modulators can make the device reflectivity arbitrarily small but not absolutely zero [1]. By designing R_T smaller than R_B , the (field-induced) absorption makes the effective reflectivity from the bottom mirror through the cavity loss equal to R_T but opposite in phase so that the net reflectivity equal zero. Since the bandwidth is determined by the resonance width at the off-level, the bandwidth of the AFP is generally wider than high-finesse Fabry-Perots that use index modulation, due to its less reflective mirrors at resonance.



Reflectivity of the AFP as a function of the cavity length product for top mirror reflectivity of 0.32 and 0.78.

Figure III.1

III.2. Low Voltage, Low Insertion Loss, and High Contrast AFPM

The AFP is composed of a pair of asymmetric mirrors separated by a low loss active spacer layer to make the net reflectivity at the resonant wavelength high at zero bias. The top mirror is made less reflective than the bottom grating. The off-level is provided by increasing the loss (e.g., electro-absorption effect) in the cavity so that the effective reflection from the bottom grating viewed through the lossy cavity cancels the reflection from the top mirror. In the original demonstration, the top mirror was simply an air-

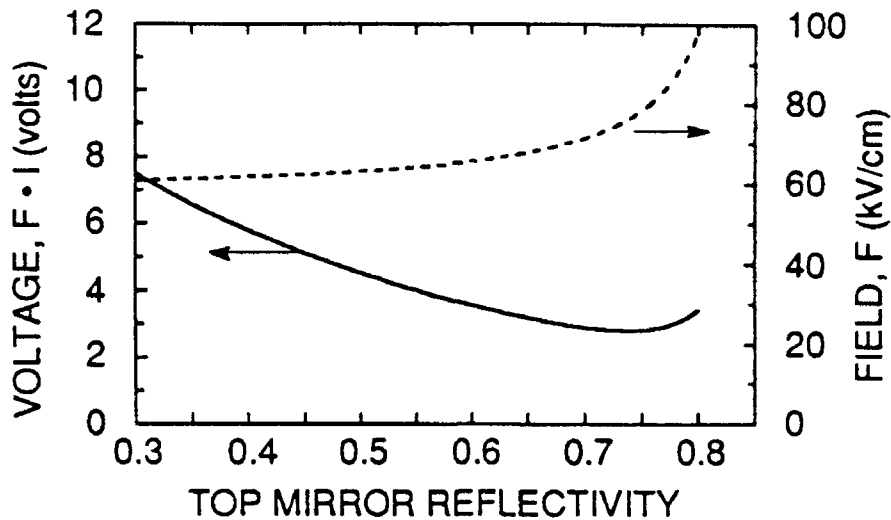
semiconductor interface for which $R_T=0.32$ [11]. The advantage of no grating mirror on top is to avoid the extra resistivity due to multiple heterojunctions, although graded junctions can reduce the resistivity [14].

As far as device design is concerned, R_T is one of the most important parameters to vary for a given material with known electro-absorption characteristics. As R_T increases, the $\alpha \cdot l$ product required to change from on to off or vice versa is decreased. For a given absorption change, the required active region thickness, l , decreases, and the applied voltage V decreases since $V \approx F \cdot l$. However, the maximum reflection decreases and the range of $\alpha \cdot l$ which gives very low reflectivity also decreases. The former effect indicates an increased insertion loss and the latter effect means that the device performance is more sensitive to design and fabrication errors.

A second factor responsible for the insertion loss is the amount of "residual" absorption when the material is at minimum loss. With the QCSE, by choosing the FP mode wavelength, λ_{FP} closer to zero-field exciton wavelength, $\lambda_{ex}(0)$, smaller fields are required to shift the exciton to the FP mode and also larger absorption can be obtained. From Eq.(2) we know that the absorber thickness, l , can be made small. However, due to the finite linewidth of the exciton, the residual loss would be quite high, and therefore also the insertion loss. Furthermore, the sensitivity increases as the top mirror reflectivity increases. Conversely, by choosing λ_{FP} away from $\lambda_{ex}(0)$, lower residual loss can be obtained to decrease the insertion loss. However, the required field and active region thickness increase, so the required voltage increases.

Using the excitonic electro-absorption model of Ref. [15], we have simulated the required voltage to achieve ≤ 3 dB insertion loss, as a function of R_T , for AFP modulators. This is given by the solid line of Figure III.9. Note that the voltage here is defined as the product of the field and the required active region thickness, $F \cdot l$. In PIN diodes, built-in voltages on the order of 1.5 volts are present, and can serve as a bias. As R_T increases, V decreases initially due to the decrease of required active region thickness. But when R_T becomes too large, the insertion loss becomes very sensitive to residual loss, and one needs to locate λ_{FP} further away from the zero-field exciton absorption edge to decrease the residual loss. As a result, larger fields, as shown by the dashed line of Figure III.2, as well as a thicker active region need to be used, and the required voltage swing increases again until the insertion loss can no longer be limited to 3 dB. The minimum voltage

happens near $R_T \approx 0.76$. Increasing the top mirror reflectivity from 0.32 to 0.78 reduces the number of quantum wells required in the active region by a factor of ≈ 3 .



The required voltage swing for the AFPM as a function of top mirror reflectivity (solid line). The required field is also shown in the dashed line.

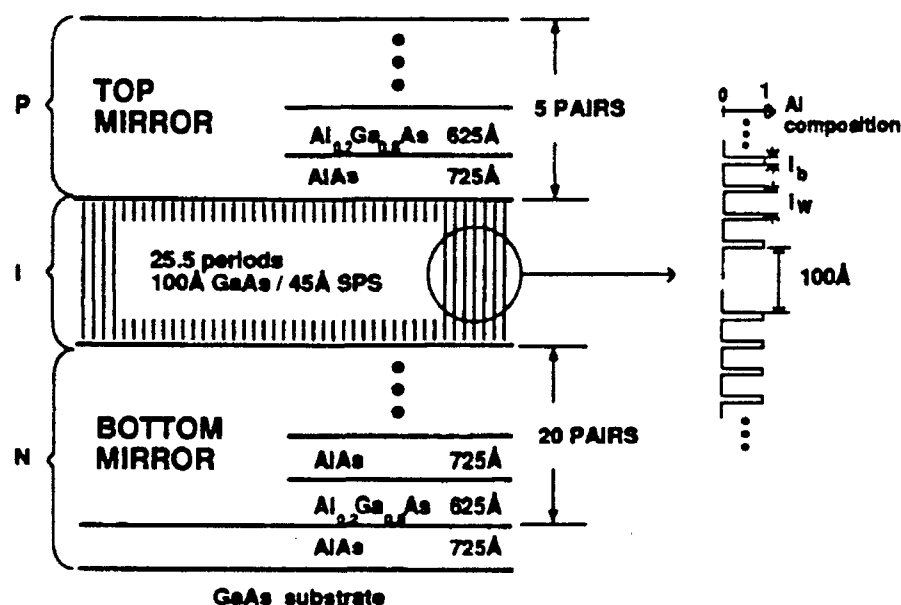
Figure III.2

The separation between the zero-bias exciton wavelength $\lambda_{ex}(0)$ and the FP mode wavelength λ_{FP} can be decreased if the QW exciton linewidth can be reduced by improved crystal growth techniques and/or a different well/barrier combination. As part of this contract, we have demonstrated that GaAs QWs confined by all-binary AlAs-GaAs short-period superlattices (SPS)[16] exhibit superior luminescent behavior and narrower luminescence linewidth due to impurity trapping by the SPS and the improvement of the interface between well and barrier, caused by the replacement of the ternary barrier material. Such high-quality QWs pose an attractive alternative to their counterparts with random alloy barriers for applications such as AFPMs and other novel optoelectronic devices.

We here summarize a normally-on transverse ASFP using QCSE in GaAs QWs confined by AlAs-GaAs SPS, embedded between a top mirror of reflectivity (R_T) $\approx 76\%$ and a bottom mirror of reflectivity (R_B) $\approx 99\%$. This is a design[17] specifically intended for low drive-voltage swing compatible with that in high-speed modern electronic circuits. The ASFP simultaneously exhibits low insertion loss ($< 1.65\text{dB}$), large reflection change

(> 68%) and practically infinite contrast at the FP resonance for an operating voltage swing of under 4V[18].

The device structure grown by molecular beam epitaxy on a (100) n+ GaAs substrate is shown in Fig. III.3. The top and bottom quarter-wave stacks consist respectively of 5 periods p-doped and 20.5 periods n-doped alternating 725Å AlAs and 625Å Al_{0.2}Ga_{0.8}As layers. The active region is composed of 25.5 pairs 100Å GaAs QWs confined by 45Å AlAs-GaAs SPS with $l_b = 3.4\text{\AA}$ and $l_w = 10.5\text{\AA}$, as schematically depicted in Fig. III.3. The application of AlAs-GaAs SPS with average Al composition of $x = 0.3$ for confinement and barrier layers minimizes all detrimental effects on the QW interfaces arising from ternary alloys. Mesa diode devices were defined by standard lithography and wet etching. Cr/AuZn/Au and AuGe/Ni/Au were then evaporated for top p-contacts and bottom n-contacts respectively. The optical window of each diode for input light illumination is 50μm x 50μm.

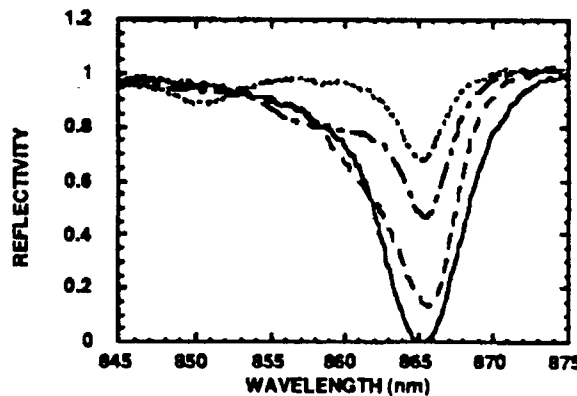


Schematic diagram of the QW-ASFP layer structure. The top and bottom mirror reflectivities are 76% and 99% respectively. The active region has 25.5 periods of undoped 100Å GaAs quantum wells confined by 45Å AlAs-GaAs short-period superlattices with $l_b = 3.4\text{\AA}$ and $l_w = 10.5\text{\AA}$.

Figure III.3

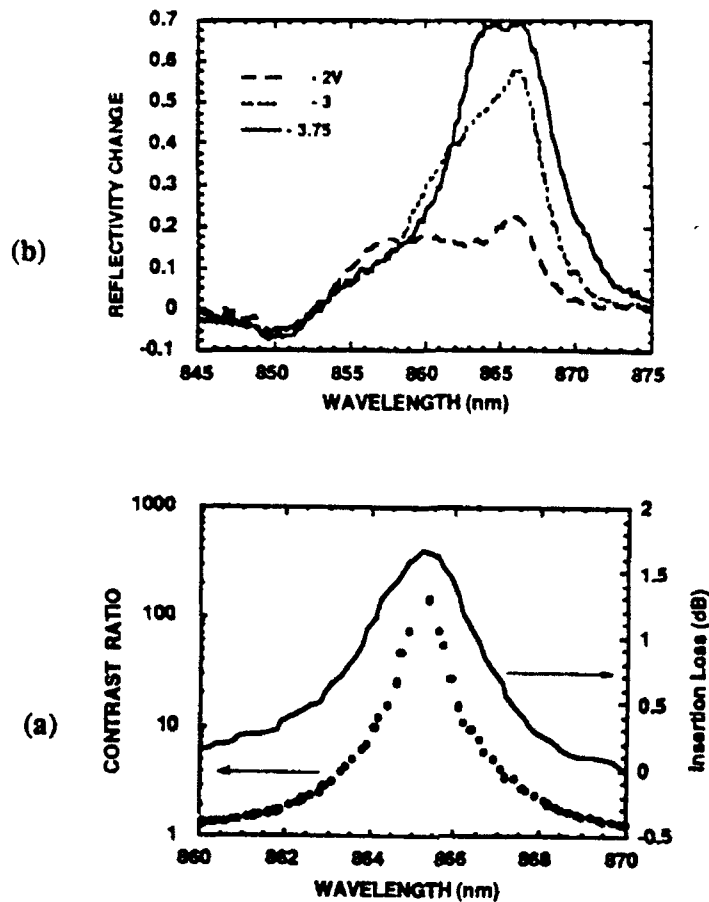
The reflectivity modulation of the device was measured by focusing light from a Ti:sapphire laser with incident power $\sim 1\mu\text{W}$ onto the QW-ASFP. Fig. III.4 shows the normalized reflection spectra for the QW-ASFP under different applied biases. $\lambda_{ex}(0)$

and λ_{FP} at zero bias are at $\sim 8500\text{\AA}$ and $\sim 8650\text{\AA}$, respectively, of which the separation is $\sim 150\text{\AA}$ ($\ll 25\text{meV}$). This is an optimal distance between the resonant mode and the zero-bias exciton for this particular ASFP structure, because it is wide enough to minimize the effect of the zero-bias QW exciton's residual absorption at λ_{FP} on the device's on-state reflectivity without increasing the operating voltage too much and reducing α_{off} to too small a value to balance the ASFP. Hence, the FP mode reflectivity (R_{FP}) decreases monotonically from $\sim 68\%$ to practically 0% as the voltage is increased from 0 to -3.75V . Small red and then blue shifts of the FP mode due to the small refractive index changes accompanying the QCSE are also observed. Both the contrast ratio $[= R(0\text{V})/R(-3.75\text{V})]$ and the reflectivity change $[\Delta R(V) = R(0\text{V}) - R(V)]$ of the QW-ASFP as a function of wavelength are shown in Fig. III.5. For a voltage swing of 3.75V , within measurement error, a practically infinite contrast ratio can be attained at $\lambda_{FP} = 8652\text{\AA}$ and a contrast ratio of more than 10:1 is observable over an optical bandwidth of $\sim 22\text{\AA}$ around the resonance. $\Delta R(-3.75\text{V})$ at the wavelength of peak contrast is $> 68\%$. Such a large reflection change at λ_{FP} with a relatively low drive voltage leads to a total reflectivity change per unit drive voltage of more than $18\%/V$. The insertion loss at λ_{FP} with peak contrast ratio is $< 1.65\text{dB}$. At the wavelengths 8641\AA and 8663\AA , which mark the spectral limits for 10:1 contrast, the insertion losses are as low as 1.17dB and 1.12dB respectively. To the best of our knowledge, this is the first ASFP that possesses the features of very low insertion loss, large reflectivity change and high contrast ratio at λ_{FP} , and only requires a low drive-voltage attainable in CMOS electronic circuits.



Narrowband modulation spectra of the QW-ASFP under various bias voltages. The reflectivity at FP resonance decreases monotonically from 68% to 0% for an operating voltage swing of only 3.75V .

Figure III.4



(a) Contrast ratio $[= R(0V)/R(-3.75V)]$ and insertion loss, and (b) change $[\Delta R(V) = R(0) - R(V)]$ in reflectivity of the device as a function of wavelength at three different bias voltages. The contrast ratios for those wavelengths with $R(-3.75V) = 0\%$ are not shown. A reflectivity change of $>35\%$ ($>50\%$ of the peak ΔR) can be observed over an optical bandwidth of $>75\text{\AA}$ which is larger than that of the contrast ratio, 22\AA , defined as the spectral width with more than 10:1 on/off.

Figure III.5

Since the AFP is operated with the electro-absorption effect of MQW's, a strong photocurrent signal is detected for all bias conditions. Note that the built-in voltage of ≈ 1.5 volts gives a field of ≈ 40 kV/cm which is sufficient to provide the bias for detection. The detector response is voltage-dependent, as expected. Since the transmission through the AFP is quite small ($\leq 3\%$), the fraction of the light that is absorbed in the active region (A) is approximately equal to one minus the reflected power relative to the input power (R), i.e. $A \approx 1-R$. So if the input optical signal carries a bit stream, the modulator can be used as a detector. Such a function has recently been demonstrated [18], and the results would be improved further with the low-voltage AFP modulators.

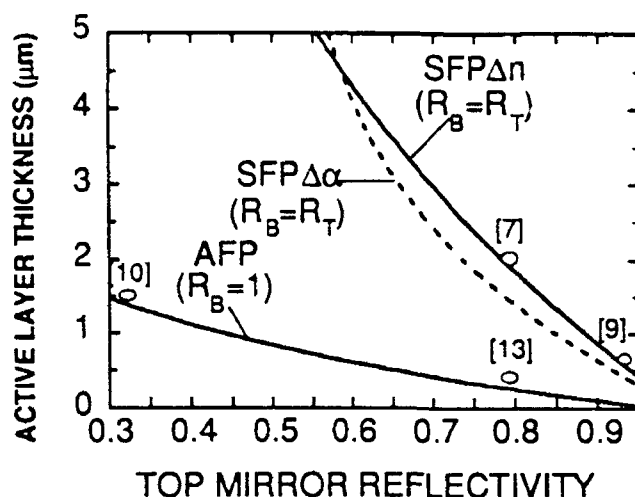
III.3. Comparison of Various Fabry-Perot Modulators

In asymmetric Fabry-Perot structures, R_T is made smaller than R_B . One could also design a structure with $R_T = R_B$, and use the loss induced in the cavity to effectively decouple the bottom mirror reflectivity. In the limit as the induced loss increased, the net cavity reflectivity would tend towards R_T . The design of the mirrors would be similar to the index-tuned Fabry-Perot (SFP Δn) modulator, in that the reflectivities would need to be high to minimize insertion loss, and the cavity would be slightly asymmetric to compensate for residual loss in the active region. We refer to this absorption-tuned quasi-symmetric Fabry-Perot as SFP $\Delta\alpha$.

To compare index- and absorption -tuned Fabry-Perot modulators, based on our previous measurements, we make the reasonable assumption that the MQW material has a maximum absorption change, $\Delta\alpha = 4000 \text{ cm}^{-1}$ and a maximum real refractive index change, $\Delta n = 0.3 \%$. Note that $(4\pi/l)(\Delta n/\Delta\alpha) = 0.4$. This being less than 1 indicates that MQW material is more efficient in electro-absorption mode than in electro-refraction mode. All devices are modeled to have 3 dB insertion loss at their on-state, and zero-reflection at the off-state.

Figure III.6 plots the required active region thickness to achieve the modulation between the on (50 %) and off (0 %) states as a function of the top mirror reflectivity. The advantage of the AFP is now obvious. SFP $\Delta\alpha$ and SFP Δn -type devices are found to be comparable in terms of the required active region thickness. Data points shown in Figure III.6 illustrate the agreement of our experiments with the simple model.

It should be noted that for the same R_T , thinner required active regions represent wider optical bandwidth BW_0 because optical bandwidths are inversely proportional to the product of the finesse and the effective cavity length, which is the sum of the actual cavity length and the grating mirror penetration length. More detailed discussions on optical bandwidths are given in Section IV.



A comparison of the required cavity length for various Fabry-Perot modulators. Actual device designs are also indicated from cited references.

Figure III.6

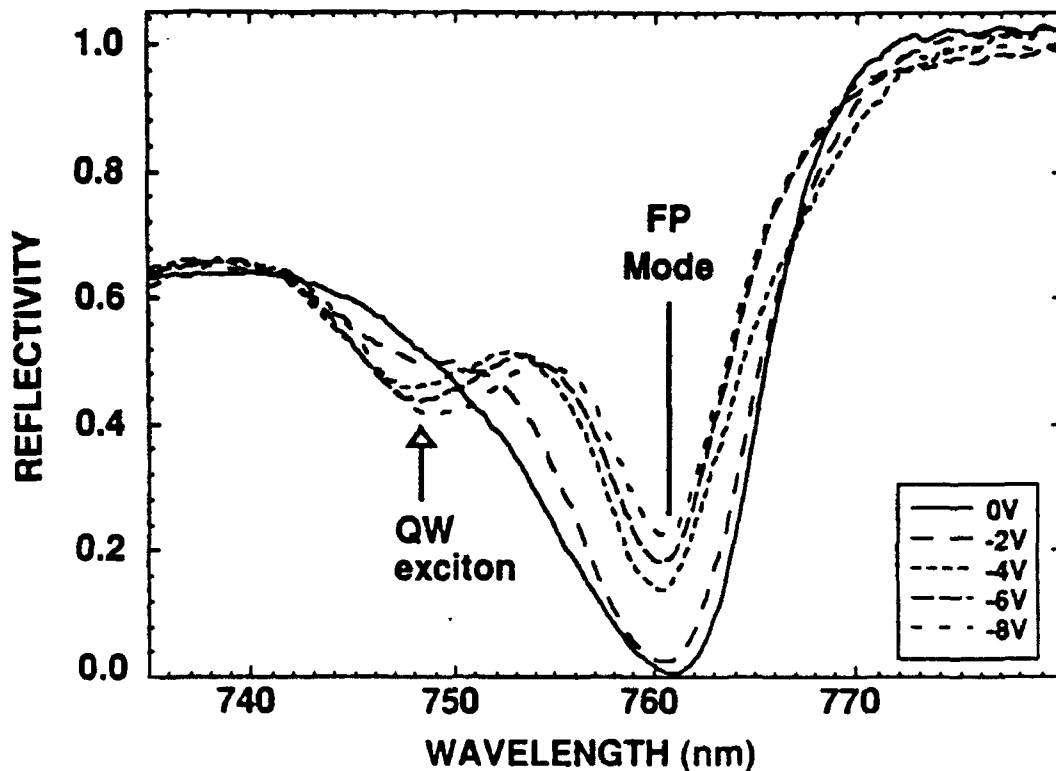
III.4. Superlattice AFPM with a Normally-Off Characteristic

Although all of the work on AFP modulators discussed in the previous sections has used the quantum confined Stark effect (QCSE) in QWs, we have also demonstrated a device which exploits the Field Induced Stark Localization effect in a superlattice (SL) [19], for which we described initial experimental results in our previous report. By "superlattice" we mean a structure where the wells and barriers are of a thickness such that the quantum-confined energy states are no longer sharply defined, but broadened into minibands in the absence of an electric field. In contrast to the absorption-edge red shift in QWs due to the QCSE, the SL absorption edge shifts to the blue with increasing field due to the localization of extended states in both conduction and valence minibands in the SL. Essentially the absorption edge sharpens up with bias. This phenomenon, generally referred to as Wannier-Stark localization [20], has been observed at room temperature [19] and potentially offers lower voltage operation than the QCSE.

Our SL-AFP [21] contains a SL (100 1/2 pairs of 30Å GaAs / 30Å Al_{0.3}Ga_{0.7}As) active layer in between a highly reflective bottom mirror, which is a quarter-wave (1/4) stack (15 1/2 periods of alternating 618Å AlAs and 535Å Al_{0.3}Ga_{0.7}As layers), and a less reflective top mirror, which is an air-semiconductor interface ($R_T \approx 0.3$). The off-level of

the SL-AFP at zero-bias is achieved by aligning the Fabry-Perot (FP) resonance at the appropriate wavelength relative to the low (or zero) field absorption edge with enough absorption so that the effective reflection from the bottom mirror viewed through the absorptive cavity cancels the reflection from the top. The on-level is attained by reducing the cavity loss using a field-induced blue shift of the SL absorption edge upon application of sufficient field.

Fig. III.7 shows the narrowband spectra of the SL-AFP device under different reverse biases. The reflectivity at the zero-bias Fabry-Perot mode increases with increasing bias and reaches a value of 25% at -8V.

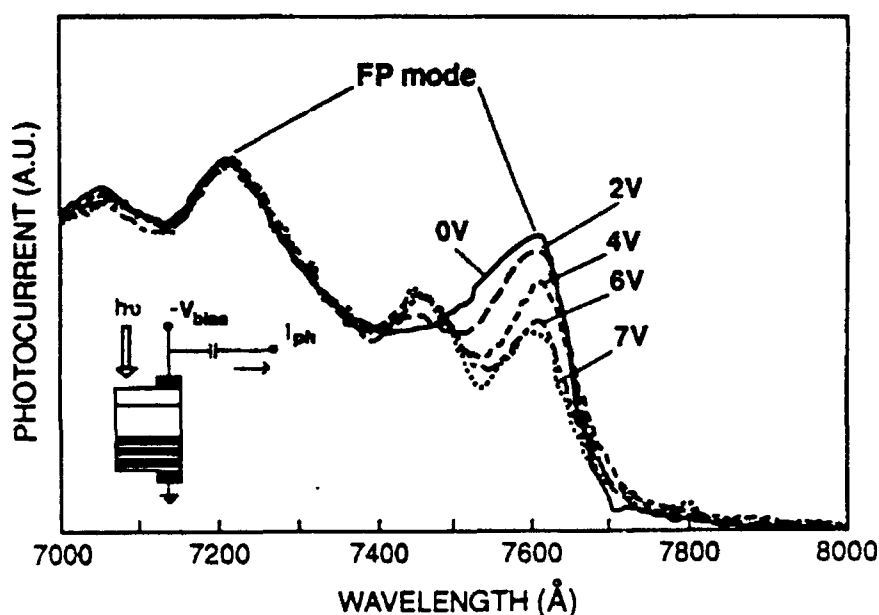


Narrowband reflection spectra of the SL-AFP device under different reverse biases.

Figure III.7

Fig. III.8 shows the photocurrent measurements of the SL-AFP as a function of wavelength at various reverse biases. The photocurrent (I_{ph}) spectra are voltage dependent as are the reflectivity counterparts. In this device, the fraction of light that is absorbed inside the cavity's active material is approximately equal to $(1-R_{FP})$ since the

transmission through the SL-AFP is only a few percent. At the zero-bias resonant wavelength ($\approx 7620\text{\AA}$), the net reflectivity R_{FP} of the SL-AFP is essentially zero when there is sufficient but not excessive loss inside the cavity. Therefore the incident light is totally absorbed and the I_{ph} is at its maximum at resonance. As the applied electric field is increased beyond the built-in value, R_{FP} is increased by reducing the cavity loss at resonance through the blue-shifted electro-absorption effect of Wannier-Stark localization in the superlattice. The I_{ph} around the resonance wavelength decreases with increasing field as a result. There is a progressive emergence of a peak at $\approx 7460\text{\AA}$ with increasing field which is due to the recovery of the QW exciton as a result of Wannier-Stark localization. Fig. III.8 shows that negative differential resistance is observable over a wide range of wavelengths ($\approx 7500\text{\AA}$ to 7650\AA). The existence of this negative differential resistance is a necessary condition for successful demonstration of a Self Electro-optic Effect Device (SEED) [22].



Photocurrent spectra of the SL-AFP at different reverse biases. The structure exhibits negative differential resistance over a wide range of wavelengths (7500\AA - 7650\AA). The inset shows the experimental schematic for the photocurrent measurement where conventional lock-in techniques were used.

Figure III.8

IV. Sensitivity Analysis

IV.1. Wavelength, Temperature, and Voltage Effects

Resonator-type devices are known to be sensitive to operating conditions. Although the AFP modulators mentioned above usually have low finesse (≤ 10), variations in wavelength, voltage, temperature will have some bearing on the stability of the device operation. We analyze these effects in this section.

In general, the AFP requires the right amount of absorption (α_{op}) induced at the right wavelength (λ_{FP}), near which wavelength (λ_{op}) the optical signal is operating. The absorption at λ_{FP} is determined by the applied field (F) and the relative wavelength shift between λ_{FP} and $\lambda_{ex}(0)$, the zero-field exciton position. Our design is to use F_{op} to shift the exciton from $\lambda_{ex}(0)$ to λ_{FP} to induce the required absorption α_{op} to turn off the AFP as given by eq.(2), i.e.:

$$\alpha_{op} = (2l)^{-1} \ln(R_B/R_T) \quad (3)$$

A variation in F and $\lambda_{ex}(0)$ would cause the induced absorption, α , to be different from α_{op} , making the off-level non-zero. The on-level would of course be changed due to these variations, but it is less sensitive than the off-level, because the latter is the one that determines the contrast ratio the most. Therefore, the sensitivity is determined by the variation of the off-level to the variations in wavelength and absorption. Variations in F are due to variations in applied voltages, while variations in $\lambda_{ex}(0)$ could be due to thermal drift of the bandgap energy.

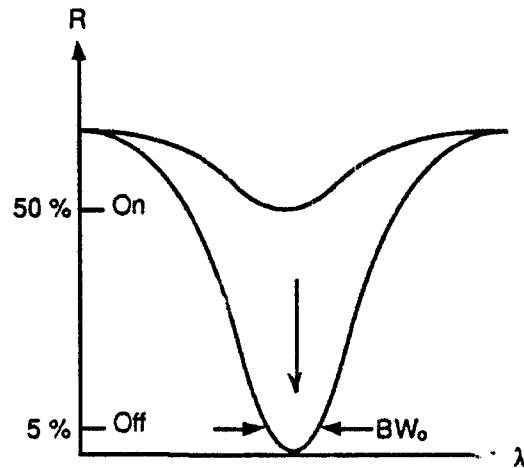
IV.1a. Operating Wavelength Variations - Optical Bandwidth

When reflection modulators are in their off-state, the reflection stays low only over a certain wavelength range, as shown schematically in the inset of Figure IV.1(a). Assuming the on-state is 50% reflective and the system requires 10 dB contrast, the optical bandwidth is the wavelength range over which R_{off} (off-state reflectivity) stays below 5%. Following the procedure in Ref. [9], we have the following expression for the allowable wavelength variation $\Delta\lambda_{op}$ with respect to λ_{FP} :

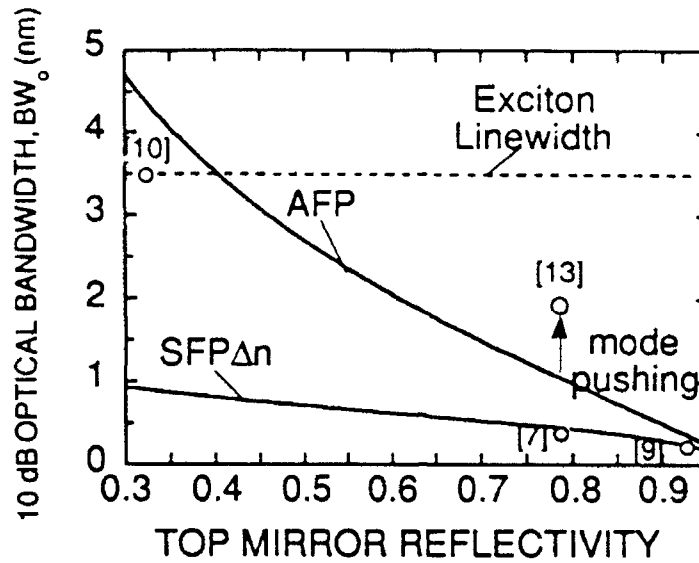
$$\Delta\lambda_{op} = \frac{\lambda_{FP}^2}{4\pi n(1 - \frac{\lambda}{n} \frac{dn}{d\lambda})(1 + L_{eff,T} + L_{eff,B})} \cos^{-1} \left[1 - \frac{(\frac{1-R_T}{2R_T})^2 R_{off}}{1 - R_{off}} \right] \quad (4)$$

where $L_{eff,T(B)}$ is the penetration depth in the top (bottom) grating, and R_{off} is the requirement on the reflection in the off-state which is set at 5% in our example. For convenience, we assume $L_{eff,T} + L_{eff,B} = 1 \mu m$, although the actual values depend on the design of the grating mirrors.

Figure IV.1(b) plots the 10 dB optical bandwidth BW_o , given by $2 \cdot |\Delta\lambda_{op}|$ based on the active region thickness requirement calculated in Figure III.6 (Section III.3). The measured optical bandwidths of various devices are also indicated. Reasonable agreements have been obtained, and therefore the optical bandwidth of Fabry-Perot type devices is mainly determined by the structure itself, rather than the material's electro-optical effect, because the optical bandwidth is somewhat smaller than the exciton linewidth. The one exception is the AFPM with $R_T = 0.32$. Because the finesse is only ≈ 2 , this device has a material-limited optical bandwidth.



(a)



(b)

(a) Schematic drawing for defining optical bandwidth. (b) Calculated optical bandwidth for SFPΔn and AFP as a function of top mirror reflectivity. Data points are also included from the indicated references.

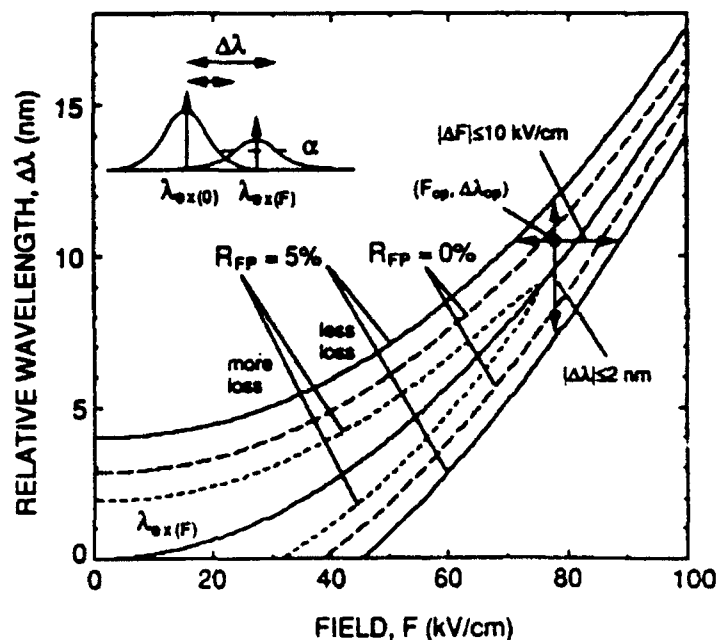
Figure IV.1

IV.1b. Voltage Swing Variations

Variations in voltage, i.e. variations in field, would cause the absorption in the MQWs at the FP mode to deviate from design values. The analysis shown in Figure IV.2 models the effect of variation of absorption on the off-level due to variations in field (F) and zero-field exciton position ($\lambda_{ex}(0)$). Wavelength variation can also be interpreted as variation in the operating wavelength or the position of the Fabry-Perot mode. So the variation in wavelength can be discussed in terms of the difference of the operating wavelength (FP mode) and the zero-field exciton position, $\Delta\lambda = \lambda_{FP} - \lambda_{ex}(0)$.

The inset of Figure IV.2 schematically shows the heavy-hole excitonic absorption as a function of wavelength under applied electric field. For a given Fabry-Perot cavity loss value, α , one can trace the contours of field and wavelength shift ($F, \Delta\lambda$) to give the same value α . Due to the Lorentzian shape of the excitonic line, there may be more than one branch of such curves. In other words, under a given field there may be more than one wavelength shift ($\Delta\lambda$) that gives α , as illustrated in the inset.

Figure IV.2 shows the absorption contours corresponding to $R_{\text{off}}=0$ and 5% for a 2V AFP modulator. The dashed lines represent the contours for $R_{\text{off}}=0\%$ (absorption=2271 cm^{-1}). Due to the Lorentzian line shapes as mentioned, there are two branches for $R_{\text{off}}=0\%$. For $R_{\text{off}}=5\%$ there are two absorption values, 1324 (less loss) and 3770 (more loss) cm^{-1} , shown in solid and dotted lines, respectively, as indicated. There are four branches for $R_{\text{off}}=5\%$. There are two zones defined by the two different absorption contours, within which zones R_{off} stays below 5%. The two zones merge where the higher loss contours stop, since the higher loss value is actually larger than the peak absorption of the exciton. This condition is satisfied when the loss contour meets the exciton peak position trace (also in solid line) as a function of field.



Sensitivity of the applied field and the zero-biased exciton position.

Figure IV.2

Our design is to locate the operating condition near the point where the two zones merge to give the most tolerable operating variations. As one can see, the merged zone gets narrower as the field or the wavelength shift increase. The experimental operating point is indicated by the dot $(F_{\text{op}}, \Delta\lambda_{\text{op}})$. It should be noted that the lower zone corresponding to the short wavelength side of the heavy-hole exciton only represents partial information. The actual situation may be more complicated due to the presence of the light-hole

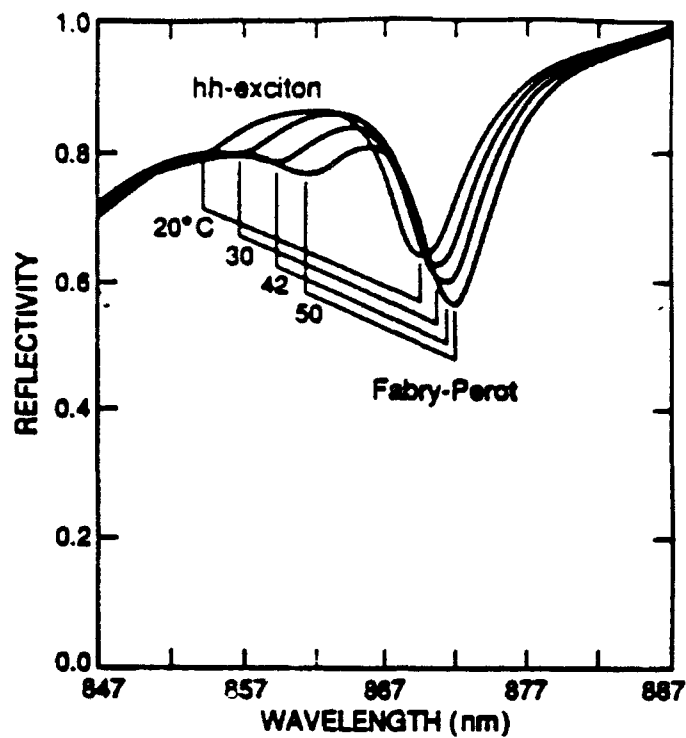
exciton and the onset of the continuum transitions. To maintain low insertion loss, $\lambda_{FP} - \lambda_{ex}(0)$ should be kept above some value due to the finite linewidth of the hh-exciton. For example, $\lambda_{FP} - \lambda_{ex}(0)$ needs to be >10 nm for maintaining less than 3dB insertion loss, although at this point we have experimentally observed ≈ 4 dB insertion loss.

When the applied field is F_{Op} , the tolerance in the wavelength shift is $\approx \pm 2$ nm, as represented by a segment of vertical line in Figure III.10 passing through the operating point to maintain $R_{off} \leq 5\%$. Note that this is the tolerance in $\lambda_{FP} - \lambda_{ex}(0)$, not in the operating wavelength. The actual tolerance in the operating wavelength is more determined by the FP mode linewidth (± 1 nm), as described in section IV.1a. Similarly, with the right wavelength shift, $\Delta\lambda_{Op}$, the tolerance in field variations is $\approx \pm 10$ kV/cm as indicated by a horizontal line segment. For a $0.5 \mu\text{m}$ thick active region, the tolerable voltage variation is ≈ 0.5 volts, which agrees with experiment. This 20% voltage tolerance represents the sensitivity of the AFP of finesse 12 to applied voltage variations.

IV.1c. Temperature Variation

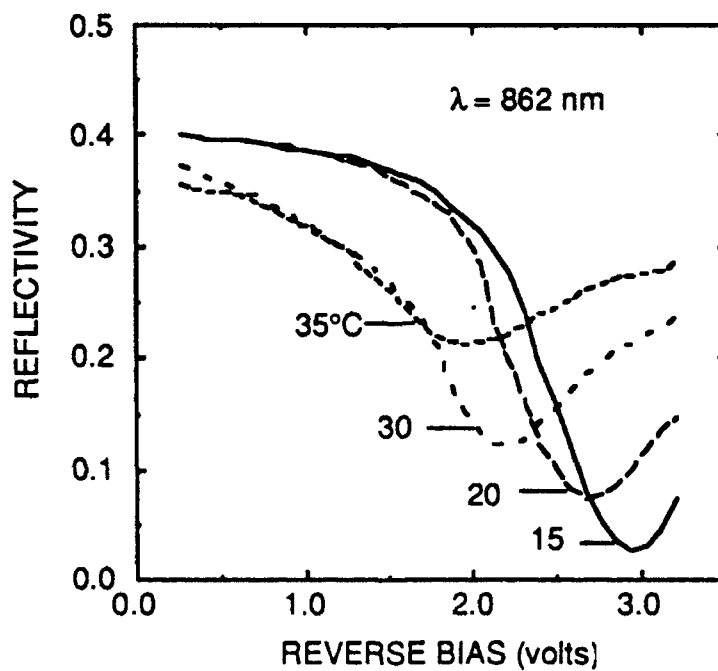
Variation in temperature causes a drift of the bandgap energy and a change of the refractive index. The former changes the exciton position while the latter varies the FP wavelength. Figure IV.3 shows the temperature-dependent zero bias reflection spectrum of the AFPM. The two reflection dips correspond to the heavy hole exciton and FP mode, as indicated. As seen from Figure IV.3, the heavy hole exciton shifts three times faster than the FP mode [23].

Figure IV.4 shows the temperature-dependent modulation of the AFPM as a function of voltage. λ_{Op} is chosen to be λ_{FP} (862 nm) at 20°C . The transfer function is smaller ($\approx 13\%/V$) than the peak value of $23\%/V$, which is observed at another wavelength. One sees immediately that as the temperature increases from 20 to 35°C , the insertion loss initially increases due to the increased residual loss caused by the approaching of the exciton. After that, the insertion loss does not vary much because λ_{Op} and λ_{FP} are no longer aligned. As the temperature increases, the separation between $\lambda_{ex}(0)$ and λ_{Op} decreases, so one does not have to apply as large a field to shift the exciton to λ_{Op} , and the required voltage to achieve minimum reflectivity decreases. Although the difference between high and low reflectivity decreases as the temperature increases, the electro-optic transfer function remains about the same, $M_V = 13\%/V$, from 15 to 30°C , and degrades a little at 35°C . However, the contrast degrades a great deal.



Temperature-dependent zero bias reflection spectrum of the ASFP.

Figure IV.3



Temperature-dependent modulation as a function of applied voltage of the ASFP. The operating wavelength is 862nm.

Figure IV.4

Due to $\Delta\lambda_{FP}$, the operating wavelength λ_{op} is misaligned with λ_{FP} and the tolerable $\Delta\lambda_{FP}$ is $\approx \pm 1$ nm or $\pm 10^\circ\text{C}$ for AFPMs. In addition to $\Delta\lambda_{FP}$, the exciton is also shifted, and $\lambda_{FP}-\lambda_{ex}(0)$ shifts at a rate of $1.8 \text{ \AA}/^\circ\text{C}$. If the operating wavelength tracks the FP mode, from the requirement of $\Delta(\lambda_{FP}-\lambda_{ex}(0)) \approx \pm 2\text{nm}$, we know that the temperature tolerance is also $\approx \pm 10^\circ\text{C}$. If the operating wavelength is fixed, the tolerance in temperature would be less than 10°C for high contrast. On the other hand, large reflectivity change can be obtained with much larger operating tolerances.

It is interesting to note that without the FP resonance, $\lambda_{ex}(0)$ determines the operating wavelength. For a fixed operating wavelength, the tolerance to temperature variations is smaller because $\frac{\partial\lambda_{ex}}{\partial T}$ is larger than $\frac{\partial\lambda_{FP}}{\partial T}$. On the other hand, if the operating wavelength tracks the exciton, the tolerance to temperature variations is much larger.

IV.2 MBE Growth Tolerances

In this section we present a study of the effects of the active cavity layer thickness variation on the operating characteristics of normally-on low-voltage high performance asymmetric Fabry-Perot modulators. For a modulator consisting of 25.5 periods of a multiple-quantum-well active region (100\AA GaAs / 45\AA (GaAs/AlAs) short period superlattices) with 5 pairs and 20.5 pairs of top and bottom quarter-wave stacks respectively (as in Fig. III.3), assuming only layer thickness variation in the active cavity caused by Ga flux nonuniformity, the shift of the Fabry-Perot mode wavelength is ~ 5.8 times that of the QW heavy-hole exciton. This affects the relative distance between the wavelengths of the quantum well exciton and the Fabry-Perot resonance, and hence the performance of the modulators. Also, the tolerable percentage change of the Fabry-Perot mode wavelength should be less than 0.13% in order that such modulator arrays have at least 10:1 contrast ratios at a fixed optimum operating wavelength. This defines the epitaxial growth tolerance for obtaining the uniformity of the operating wavelength of an array and the precision with which we can obtain a desired wavelength, its reproducibility, and its uniformity across a wafer.

As discussed above, it is desirable for a surface-normal optical modulator to exhibit both high contrast ratio and low insertion loss. For an ASFP to achieve simultaneously the lowest insertion loss possible and an infinite contrast ratio tight control of epitaxial layer

thicknesses and compositions is required. The need to match the quarter-wave stack spectral response and the effective cavity length in order to place λ_{FP} at an optimal distance from $\lambda_{ex}(0)$, along with the different rates of variation of λ_{FP} and $\lambda_{ex}(0)$ with layer thickness and composition, make this crucially important. In addition, because of the finite linewidth of the FP resonance, spatial variations of λ_{FP} will cause variation of optimum operating wavelength among devices from different areas of a wafer. In order to investigate the feasibility of fabricating a reasonably sized array of ASFPs with uniform usable operating characteristics, in this work, we examine one aspect of the problem: the QW-ASFP's sensitivity to the active layer thickness and/or composition variation. This defines the epitaxial growth tolerance for obtaining uniformity of the operating wavelength of an array and the precision with which we can obtain a desired wavelength, its reproducibility, and its uniformity across a wafer.

Consider an FP cavity of length L_c clad by two different distributed Bragg reflectors (DBRs) as shown in Fig. IV.5. In the vicinity of the Bragg frequencies of the DBRs, the reflectivity of each mirror is assumed to have uniform amplitude and a linear phase; the complex amplitude reflectivity of the top (bottom) mirror is given by [24]:

$$\tilde{r}_{1(2)}(\omega) = r_{1(2)} \exp(j\phi_{1(2)}(\omega)) \quad (5)$$

where $r_{1(2)}$ is the peak amplitude reflectivity at the mirror Bragg frequency $\omega_{1(2)}$ and $\phi_{1(2)}$ is the frequency-dependent phase of reflection. Without loss of generality, the Bragg frequencies of the two mirrors can be assumed to be equal, i.e. $\omega_1 = \omega_2 = \omega_B$ and the phases of the mirrors at can be assumed to be 0. Therefore, by defining the penetration depth in the two DBRs as:

$$L_{\tau_{1(2)}} = \left(\frac{\lambda_B^2}{4\pi\bar{n}} \right) \left(\frac{\partial \phi_{1(2)}}{\partial \lambda} \right)_{\lambda=\lambda_B} \quad (6)$$

where \bar{n} is the average refractive index inside the active medium and $\lambda_B = 2\pi c/\omega_B$, λ_{FP} is given by:

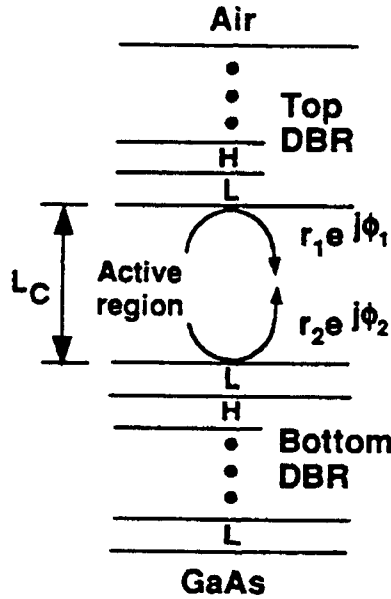
$$\lambda_{FP} = \frac{2\bar{n}(L_c + L_{\tau})}{m + 2\bar{n}L_{\tau}/\lambda_B} \quad (7)$$

where m is the order of the FP mode and $L_\tau = L_{\tau 1} + L_{\tau 2}$. If there is a perturbation in the optical length of the active region, i.e. $\Delta(\bar{n}L_c)$, then the change in the FP mode wavelength ($\Delta\lambda_{FP}$) is:

$$\frac{\Delta\lambda_{FP}}{\lambda_{FP}} = \left(\frac{L_c}{L_c + L_\tau}\right) \left(\frac{\Delta(\bar{n}L_c)}{\bar{n}L_c}\right) \quad (8)$$

If the change of λ_{FP} is due only to a variation of L_c , then taking into account of index dispersion of the active medium, (8) can be written as:

$$\frac{\Delta\lambda_{FP}}{\lambda_{FP}} = \left(\frac{L_c}{L_c + L_\tau}\right) \left(\frac{\Delta L_c}{L_c}\right) / \left(1 - \frac{L_c}{L_c + L_\tau} \frac{\lambda}{\bar{n}} \frac{\partial \bar{n}}{\partial \lambda}\right) \quad (9)$$



Schematic illustration of a generic ASFP structure. $r_1(2)\exp(j\phi_1(2))$ is the complex amplitude reflectivity of the top (bottom) mirror, where ϕ_1 and ϕ_2 are the frequency dependent phases of the reflection of the top and bottom mirrors respectively. L_c is the length of the active region. Each component layer of both DBRs is of thickness one quarter of the Bragg wavelength.

Figure IV.5

Since, for GaAs at photon energy below the band edge, $\partial \bar{n} / \partial \lambda$ is negative, the effective $\Delta\lambda_{FP} / \lambda_{FP}$ is smaller than it would have been without index dispersion. It should be noted that the change in $\bar{n}L_c$ due to composition variations will have the same effect as adding or subtracting a certain thickness of material. In this study, the barrier material of

the QWs in the active region of the ASFP is composed of AlAs/GaAs short period superlattices (SPSs), in place of an AlGaAs alloy, for the sake of improving QW interfaces (Fig. IV.5). In this case, the fractional change of λ_{FP} will be:

$$\frac{\Delta\lambda_{FP}}{\lambda_{FP}} = \left(\frac{L_c}{L_c + L_\tau}\right) \left(\frac{\Delta(n_A L_A) + \Delta(n_G L_G)}{\bar{n} L_c}\right) \quad (10)$$

In (10), $\bar{n} L_c$ is assumed to be equal to $n_G L_G + n_A L_A$, where n_G and n_A are the refractive indices of GaAs and AlAs, and L_G and L_A are the total thicknesses of GaAs and AlAs, respectively. Since the active medium contains only binary compounds, $\Delta\lambda_{FP}$ will be a function of thickness variations of the constituent layers only. The index dispersion relationships of both component layers can also be included into (10) as was done in (9).

If there is also a small systematic departure from a quarter-wave in every component layer of both DBRs, in addition to variation in $\bar{n} L_c$, the mirror reflectivities in the stop-bands of the mirrors will not be much affected because the reflectivity in the high-reflection band of each mirror changes very little and the dominant effect is the change of phase. Assuming the FP mode still occurs in the linear phase regions of both DBRs (which is the case of interest), then the fractional variation of the mode wavelength can be expressed as:

$$\frac{\Delta\lambda_{FP}}{\lambda_{FP}} = \left(\frac{1}{L_c + L_\tau}\right) \left(\frac{L_c \Delta(\bar{n} L_c)}{(\bar{n} L_c)} + \frac{L_\tau \Delta(n_i t_i)}{(n_i t_i)}\right) \quad (11)$$

where $\Delta(n_i t_i)/(n_i t_i)$ is the systematic fractional error of each quarter-wave layer optical thickness that shifts the Bragg wavelengths of the DBRs from λ_B to $\lambda_B + \Delta\lambda_B$, where $n_i t_i = \lambda_B/4$ and $i = H, L$ (Fig. IV.5). If there is an arbitrarily small departure from a quarter-wave, in the optical thickness of a particular layer or some layers of either one or both DBRs in an FP etalon, the contribution of the mode shift due to the phase error caused by this stack layer error can also be calculated but will be treated elsewhere[25,26].

Since the QW hh exciton transition energy also shifts as the well width changes, it is interesting to compare the rate of shift of the FP mode with respect to the Group III flux variations to that of the QW transition energy. By assuming the QW barrier to be of infinite height, and using the appropriate infinite-barrier well width to obtain the same

zero-field energy as the actual finite well, a closed form for the QW transition energy can be written as:

$$E_{QW} = \frac{\hbar^2}{8L_{z,\infty}^2} \left(\frac{1}{m_e} + \frac{1}{m_{hh}} \right) + E_g \quad (12)$$

where $L_{z,\infty}$ is the equivalent GaAs well width with infinite barrier height, E_g is the bandgap of GaAs, and m_e and m_{hh} are the electron and heavy hole effective masses respectively. The change in E_{QW} , due to a variation of $L_{z,\infty}$, is therefore given by:

$$\frac{\Delta\lambda_{QW}}{\lambda_{QW}} = \left(\frac{E_{QW} - E_g}{E_{QW}} \right) \left(\frac{2\Delta L_{z,\infty}}{L_{z,\infty}} \right) \quad (13)$$

where $\lambda_{QW} = hc / E_{QW}$ and h is Planck's constant.

Thus the shift of the FP mode wavelength relative to that of the QW hh exciton, due to GaAs thickness variation is:

$$R_{FP/QW} = \frac{\Delta\lambda_{QW}}{\lambda_{QW}} = \frac{1}{2} \left(\frac{L_c}{L_c + L_t} \right) \left(\frac{E_{QW}^2}{(E_{QW} - E_g)E_{FP}} \right) \left(\frac{\Delta(\bar{n}L_c)}{\bar{n}L_c} \right) \left(\frac{L_z}{\Delta L_z} \right) \quad (14)$$

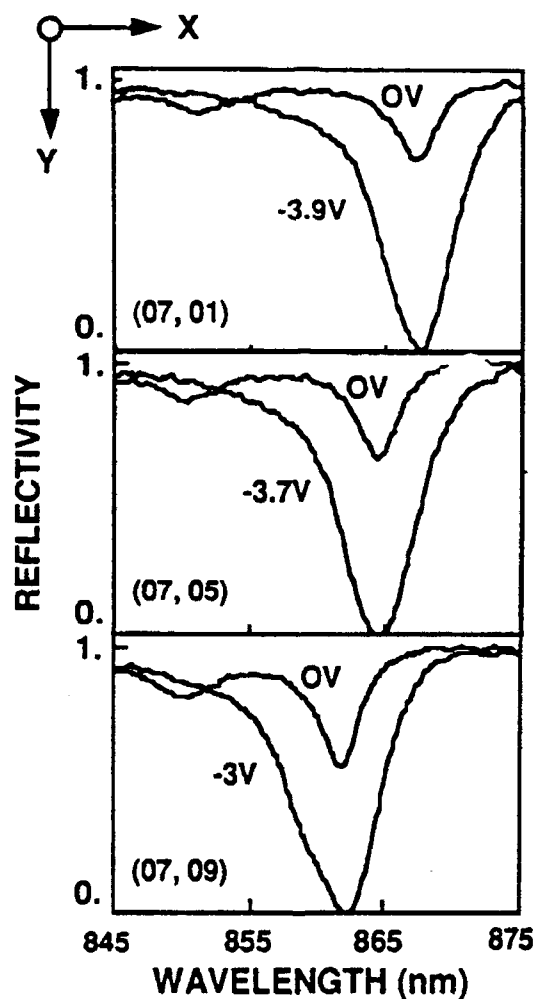
where $E_{FP} = hc / \lambda_{FP}$. And the fractional change in $L_{z,\infty}$ (i.e. $\Delta L_{z,\infty}/L_{z,\infty}$) is replaced by $\Delta L_z/L_z$, where L_z and ΔL_z are the actual GaAs well width and thickness variation, respectively. Given the device structure in Fig. IV.5, if we assume that the layer thickness variation in the cavity is due to Ga flux variation, then $\Delta\lambda_{QW}$, $\Delta\lambda_{FP}$ and $R_{FP/QW}$ can be calculated using (9)-(14). In the estimation of $\Delta\lambda_{FP}$ and $R_{FP/QW}$, the index dispersion relation of GaAs below band-gap with photon energy, $1 - (\lambda/n)(\partial n/\partial \lambda) = 1.14$ was applied. Our model predicts $\Delta\lambda_{FP}/\lambda_{FP} \approx 0.275 \Delta L_z/L_z$ and $\Delta\lambda_{FP}/\lambda_{FP} \approx 0.048 \Delta L_z/L_z$, yielding $R_{FP/QW} \approx 5.8$. If, in addition, Al flux spatial nonuniformity is also included, then λ_{QW} will essentially be unaffected, while $\Delta\lambda_{FP}$ and hence $R_{FP/QW}$ will be altered as (L_c) in (10) is increased or decreased accordingly. For example, if $|\Delta(nGLG)| = |\Delta(nALA)|$, $\Delta\lambda_{FP}$ due to the variation in Al content will be about 8% of that due to the variation in Ga only. Furthermore, if there are optical thickness variations of the quarter-wave stacks constituting the mirrors, $\Delta\lambda_{FP}$ will be changed due to this additional variation but λ_{QW} will remain the same and hence $R_{FP/QW}$ will be different from the one calculated above.

The device structure was grown by a Varian Gen II molecular beam epitaxy (MBE) system under an As₄-rich condition. Both top and bottom mirrors were grown with rotation to improve the spatial uniformity of their spectral response. The active region is composed of 25.5 periods of 100Å GaAs QWs confined by 45Å AlAs/GaAs SPSs (3.4Å AlAs and 10.5Å GaAs) (Fig. IV.5). The application of AlAs-GaAs SPS with average Al composition of $x=0.3$ for confinement and barrier layers is expected to minimize all detrimental effects on the QW interfaces arising from ternary alloys. In order to perform a spatial assessment of optical nonuniformity of the devices as a function of active cavity layer thickness and to verify the formulations derived in previous section, the wafer was not rotated during the growth of the QWs. The substrate was positioned in the MBE chamber with its major flat at an angle of $\sim 90^\circ$ ($\sim \pm 4^\circ$ due to the uncertainty in mounting the wafer on the Mo block) relative to the direction of Ga source. The devices in an array were then defined photolithographically on the central portion of the wafer. The rows (columns) of the devices were aligned parallel (orthogonal) to the wafer's major flat. Standard etching and metallization techniques, using Cr/AuZn/Au for p-contacts and AuGe/Ni/Au for n-contacts, were used for fabricating the mesa diodes. The optical window of each mesa diode for coupling input light is $50\mu\text{m} \times 50\mu\text{m}$. Center-to-center spacings of the modulators in the x-direction (row) and y-direction (column) are $250\mu\text{m}$ and $200\mu\text{m}$, respectively.

A 14×10 array of QW-ASFPs was tested by focusing light from a Ti:sapphire laser with incident power of $\sim 1\mu\text{W}$ onto the optical window of each device. The detailed reflectivity modulation of devices in every other row and every other column were measured. High contrast modulation operation of all of the devices was observed as expected though at somewhat different operating wavelengths because of the different FP mode wavelengths.

All of the devices tested in the array exhibited $>100:1$ contrast ratio with $<3\text{dB}$ insertion loss at the corresponding FP modes for operating voltage swings of less than 4V. The nonuniformity of the modulation characteristics of the devices in the array due to variations in $(\lambda_{\text{FP}} - \lambda_{\text{ex}}(0))$ and λ_{FP} is illustrated in Fig. IV.6, where, for simplicity and for purposes of illustration, the modulation spectra (on-state at 0V and off-state at optimum bias) of devices in every fourth row of the seventh column of the array are shown. The device (07,05) is a typical device having optimum separation ($\sim 150\text{\AA}$) between λ_{FP} and $\lambda_{\text{ex}}(0)$. It simultaneously exhibits low insertion loss ($<1.65\text{dB}$) and

practically infinite contrast at λ_{FP} and only requires less than 4V voltage swing. A contrast ratio of more than 10:1 is observable over an optical bandwidth of $\sim 22\text{\AA}$ around the resonance which defines the layer thickness tolerance for an array of devices with similar performance at a fixed operating wavelength.



Reflection spectrum (on-state at 0V and off-state at optimum bias) of every fourth device of every seventh column is shown. The modulators in the y-direction exhibit linear shifts of both FP mode and exciton to shorter wavelengths.

Figure IV.6

Devices in the same row are quite uniform in both $\lambda_{ex}(0)$, λ_{FP} , drive voltage, on/off ratio and insertion loss. For devices in the same column, owing to the deliberate positioning of the wafer during the QW growth such that the angle between the y-direction and the direction of Ga source is $\sim 0^\circ$, this results in a variation of L_c that is almost entirely due to thickness variation of GaAs. As shown in Fig. IV.6, devices in the

same column (in y-direction) exhibit linear shifts of both FP mode and exciton to shorter wavelengths since the thickness gradient over a small distance is linear. The relative shift, $R_{FP/QW}$, estimated from the spectra is ~ 5.5 which is in reasonably good agreement with that derived using (14), given the error in estimating the small shifts of $\lambda_{ex}(0)$. Since λ_{FP} shifts about 5.5 times faster than $\lambda_{ex}(0)$, the residual losses at the corresponding FP modes increase as the FP modes approach the hh exciton. Typically the insertion loss increases from ~ 1.5 dB (corresponding reflectivity change $(\Delta R) \geq 70\%$) at the FP mode in the first device to ~ 2.6 dB (corresponding $\Delta R \approx 55\%$) in the 10th device in a column. The magnitude of drive voltage needed to turn off a modulator in a column also drops from ~ 3.9 V in the first row to slightly less than 3.0 V in the 10th row.

All the devices tested in the array still possess less than 3 dB insertion loss and more than 20 dB contrast, despite the variation in $(\lambda_{FP} - \lambda_{ex}(0))$ being as large as ~ 45 Å. For device applications which require two-dimensional arrays of ASFPs, such as spatial light modulators for optical computing, the operating wavelength is normally fixed. The allowable FP mode wavelength variation (defined by the optical bandwidth for $\geq 10:1$ contrast[3]) which is therefore $\sim \pm 11$ Å (i.e. $\Delta\lambda_{FP}/\lambda_{FP} \approx 0.13\%$) is much smaller. This imposes the ultimate layer thickness accuracy and uniformity requirement on these two-dimensional arrays. This constraint means that the error in the optical length of the active cavity should be controlled to within 0.4%. If the optical thicknesses of the component layers of both DBRs also vary proportionately (i.e. $\Delta(\bar{n}L_c)/(\bar{n}L_c) = \Delta(\bar{n}_i t_i)/(\bar{n}_i t_i)$, $i = H, L$ in Fig. 1) then the allowable percentage error in the optical thicknesses of all the layers should be within $\sim 0.13\%$ [5].

In summary, we have studied the effects of the active cavity layer thickness and/or composition variations on the operating characteristics of normally-on low-voltage high performance asymmetric Fabry-Perot modulators. For the modulator structure that we employed, consisting of 25.5 periods of 100 Å GaAs quantum wells confined by 45 Å (GaAs/AlAs) SPS with 5 pairs and 20.5 pairs of top and bottom quarter-wave stacks, respectively, the shift of the Fabry-Perot mode wavelength is ~ 5.8 times that of the QW heavy-hole exciton, assuming only layer thickness variation caused by Ga flux nonuniformity. This affects the relative distance between the wavelengths of the quantum well exciton and the Fabry-Perot resonance, and hence the performance of the modulators. Furthermore, the tolerable percentage change of the Fabry-Perot mode wavelength should be less than $\sim 0.13\%$ in order that such modulator arrays have at least 10:1 contrast ratios at a fixed optimum operating wavelength. This, in turn, defines the

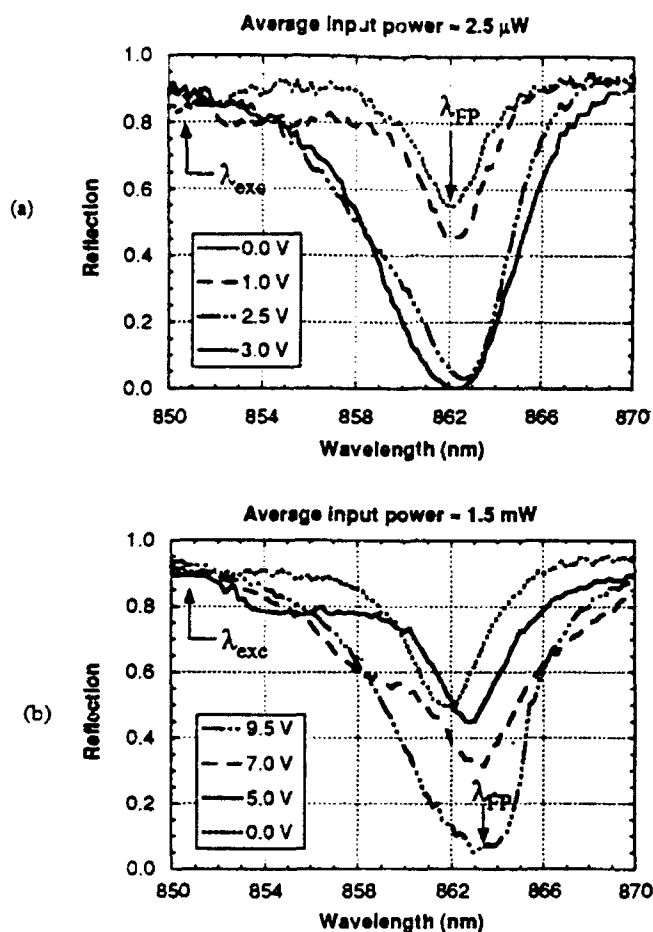
epitaxial layer and composition tolerance of the active layers which should be limited to less than 0.4% [$\sim 0.13\%$ if the variations of the optical thicknesses of the layers constituting the mirrors are taken into account and the fractional optical thickness variation of the active cavity is equal to that of each constituent layers of the mirrors (i.e. $\Delta(\bar{n}L_c)/(\bar{n}L_c) = \Delta(n_i t_i)/(n_i t_i)$, $i = H, L$) for obtaining the required uniformity of the operating wavelength of an array and the precision with which we can obtain a desired wavelength, its reproducibility, and its uniformity across a wafer.

IV.3. Power Saturation Limitations

The high-efficiency asymmetric Fabry-Perot modulator may be considered as an optoelectronic interface element for interconnection applications such as smart pixels. Due to the asymmetry of the cavity, which forces light that is not reflected to be almost totally absorbed, the device can play a dual role: as a transmitter with modulated bias and a c.w. optical input, or as a receiver with fixed bias and modulated optical input. Of course, this dual functionality is attractive, but it can be anticipated that the presence of large numbers of photo-generated carriers within the active region will ultimately begin to degrade the modulator performance through exciton screening [27] and space charge effects [28]. Furthermore, the dissipated electrical power may well lead to thermal problems. Given that we would want to fan out the modulated optical power reflected from the ASFP to a number of other devices in a 2-D array, and allowing for inefficiency of the optics, we may well require the ASFP average output to be on the order of mWatts, e.g. 50×10^{-6} W per channel into 16 channels, in order to achieve acceptable bit error rates. With this in mind, we have made some preliminary investigations of the power-dependent performance of the ASFP modulator/detector.

Figure IV.7(a) shows the spectral response of the ASFP under very low power illumination ($\approx 0.25 \mu\text{W}$). Measurements were made at room temperature under cw illumination from a tunable Ti:sapphire laser at normal incidence using the facility described later in this report. The devices were simple mesa p-i-n structures, $150 \times 100 \mu\text{m}$ in area, with a $50 \times 50 \mu\text{m}$ square window. The laser spot was estimated to be $\approx 10 \mu\text{m}$ in diameter. As described in section III.2, at the resonant wavelength contrast is more than 20dB for only $\approx 3.75\text{V}$ bias. In this particular case the voltage for maximum contrast is further reduced since the cavity resonance is $\approx 3\text{nm}$ closer to the MQW absorption edge.

Now note the changes when the input power is increased to ≈ 1.5 mW, as shown in Figure IV.7(b). We find that substantially higher voltages are required to shift the MQW absorption peak out to the FP resonance wavelength. Maximum contrast is now achieved for 9.5V, at a slightly longer wavelength than for the low power case, and it is no longer ≥ 20 dB. Additional measurements show that we can still achieve ≈ 20 dB contrast at optical powers up to ≈ 250 μ W, where the bias required increases to ≈ 5.5 V.



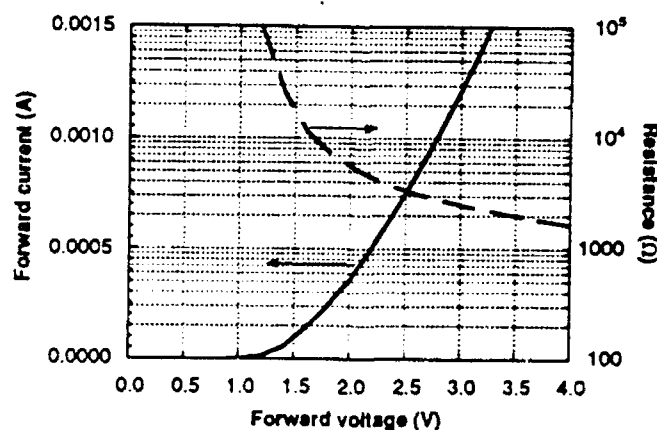
Measured reflection spectra for high-efficiency ASFP modulator at (a) low and (b) high incident optical power. Corresponding optical intensities are (a) $3\text{W}/\text{cm}^2$, and (b) $2\text{kW}/\text{cm}^2$.

Figure IV.7

We attribute the increase in the minimum reflection to a reduction in the peak absorption, due to a high density of photo-generated carriers which, even at high fields, remain within the quantum wells long enough to screen the formation of excitons to some degree [29]. Note that the minimum which occurs in the zero-volt, low power reflection curve at \approx

851nm in Figure IV.7(a), due to the exciton absorption peak at the band edge, is not visible in the corresponding high power curve in Figure IV.7(b). The screening effect is particularly strong at low biases, and has previously been observed in MQW structures at intensities of $\approx 1\text{ kW.cm}^{-2}$ [29]. The limiting factor here is the escape time from the quantum well, which can be reduced by using thinner, lower barriers and even designing to achieve resonant tunneling between adjacent wells at some specified voltage [30].

The more obvious problem is the increase in the bias voltage and the shift of the FP resonance. We believe this can be avoided by reducing the very high series resistance in the quarter-wave mirror stacks. In this particular device structure the quarter-wave stack mirrors have abrupt heterointerfaces and double as the p and n contact layers. The multiple heterointerfaces of the mirror stack present a serious hinderance to carrier transport, especially for holes in the p-doped mirror. Figure IV.8 shows the measured forward I-V characteristic for the ASFP diode. The series resistance is in the $\text{k}\Omega$ to $\text{M}\Omega$ range. For currents on the order of 1mA, which we generate for the high power case here, the associated voltage drop appears to be $\approx 2.5\text{--}3.0\text{ V}$. This also gives rise to high power dissipation within the device and thus a temperature increase which tends to shift both λ_{FP} and λ_{ex} to longer wavelengths.



Measured forward I-V characteristic and resistance of the ASFP under zero illumination.

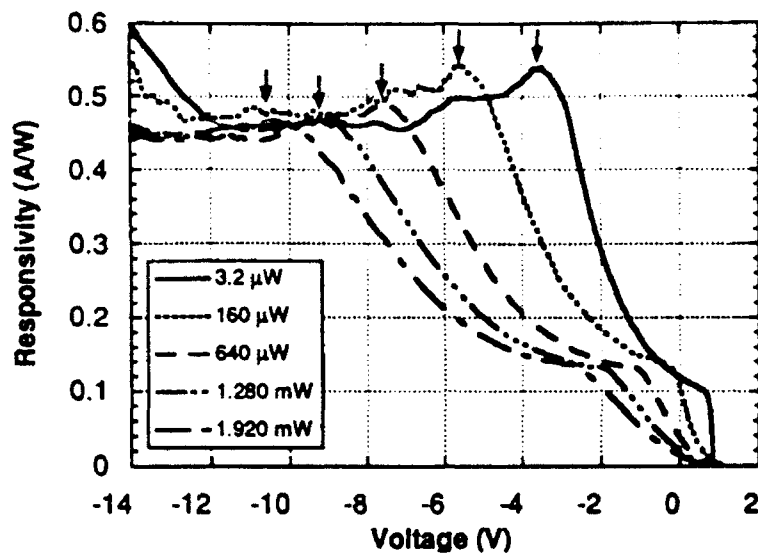
Figure IV.8

It is clear that the device characteristics are severely modified by the presence of this large nonlinear series resistance. However, this should not be a fundamental limit on the device. By redesigning the structure to incorporate intra-cavity contact layers [31] we

can avoid the problems of transport through the mirror stacks, at the expense of increased cavity width and thus reduced FP linewidth. Alternatively, we can modify the stacks themselves, with spike doping and interface grading [32] to reduce the series resistance to acceptable levels.

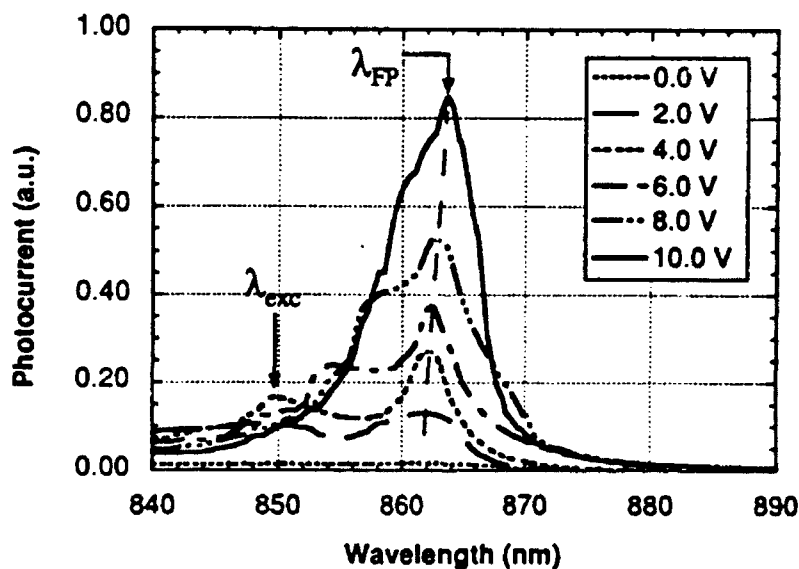
Looking at the detection properties of this ASFP structure, we find efficient responsivity over a range of optical powers up to $\approx 2\text{mW}$ at the FP resonance wavelength (862.2nm). The theoretical maximum responsivity, assuming all incident power is absorbed, and all carriers are collected in the contacts, is $\approx 0.68\text{ AW}^{-1}$. Figure IV.9 shows that at μW power levels the responsivity climbs rapidly, corresponding to a fall in the reflected power, as bias is increased so as to provide the critical amount of absorption needed to balance the cavity. Peak responsivity is $\approx 0.54\text{ AW}^{-1}$ - an impressive figure considering that the absorbing region is only $\approx 0.35\mu\text{m}$ thick. Following the trend in the reflection data, as the incident power is increased the voltage required for peak responsivity increases dramatically. As one may expect, at $\approx 1.5\text{ mW}$ the voltage for maximum current is close to 9.5V , just as for maximum contrast in the modulator. The peak responsivity is reduced compared to that observed at low power primarily because we chose to fix the input at the wavelength of maximum contrast for low power. Additional measurements have been made on an MQW p-i-n with the same active region as the ASFP, but with no cavity structure and low resistance contact layers. These showed no significant shift of the responsivity peak until the input power reached $\approx 10\text{mW}$, after which point the peak shifted to lower voltage. This is actually the expected behavior in the absence of very high series resistance, where power dissipation causes a temperature rise, pushing the MQW absorption edge toward the measurement wavelength.

For completeness, Figure IV.10 illustrates the narrow band nature of the high-efficiency photodetection in the ASFP. The input power is roughly the same as that used for the high power reflection measurements. At 0.0V it appears that the built-in field is insufficient to sweep out much of the photo-induced charge. $2\text{-}4\text{V}$ bias is required to begin to eject carriers from the quantum wells, at which point the exciton absorption peak becomes visible at $\approx 850\text{nm}$. With increasing bias the photocurrent in the neighborhood of the FP resonance increases ever quicker, with the spectral shape appearing as the inverse of the reflection spectra. Beyond 10V bias the peak photocurrent decreases very little since the absorption is then sufficient to almost balance the cavity over a wide range of bias.



Measured responsivity of the high-efficiency ASFP modulator at 862.2nm. The arrows indicate the shift of the peak responsivity to higher voltage with increasing optical power.

Figure IV.9



Photocurrent spectra for the ASFP at an input power of 1.6mW. λ_{FP} denotes the position of the FP cavity resonance. λ_{exc} denotes the excitonic absorption edge of the MQW material.

Figure IV.10

To conclude this section, we have determined that the ASFP, which was shown to operate very efficiently at low input optical powers, has some limitations in its present form at practical power levels. High series resistance must be eliminated or avoided in order for the device to operate with high contrast and low voltage at high optical power levels. This is also a prime consideration in the high speed operation of these devices. Setting aside the series voltage drop problem, we see reduction of the contrast at powers of $\approx 1.5\text{mW}$ ($\approx 2\text{kW.cm}^{-2}$). The upper limit such that we still get $\approx 20\text{dB}$ contrast is only $\approx 250\mu\text{W}$ (or $\approx 330\text{W.cm}^{-2}$). In order to improve on this figure we must re-design the barriers of the MQW region for faster sweep-out. The present short-period superlattice design, presents a high effective barrier height, resulting in the very high absorption ratios which allow us to demonstrate high efficiency at low powers. Fox et al[29], and Morgan et al[30] have recently demonstrated improvements in absorption saturation intensities to $10\text{-}60\text{ kW.cm}^{-2}$ by reduction of barrier height and width, and field-induced resonant tunneling in order to reduce carrier sweep-out time from quantum wells. Such modifications will necessarily force us to incur some increased operating voltage, or increased insertion loss in order to maintain high contrast.

Photodetection is not as sensitive a problem as reflection modulation in the ASFP. Input powers which reduce the maximum contrast from 20dB or greater to $\approx 10\text{dB}$ only reduce the responsivity by perhaps 10% .

IV.4. Power Dissipation Considerations for Arrays

A major consideration for the use of modulators in arrays is the issue of power dissipation. It is a fairly straightforward task in the case of the "optimally designed" AFPMs to calculate the power dissipation because they are characterized by a back power reflectivity of $R_B = 1$, and therefore all optical power is either absorbed or reflected. These modulators have typical contrast ratios of $>20\text{db}$, which means that the power reflected in the off state is below 1% and therefore the power absorbed is approximately equal to the incident power. In addition to the optical power absorbed, one must add the electrical power dissipated by the device due to photocurrent. The QW modulators which are based on the QCSE are normally-on devices (as opposed to the superlattice devices based on the Wannier Stark effect, which are normally-off devices) and the applied voltage in the "on" state is normally $V_A = 0\text{V}$. In this case, the power dissipated due to photocurrent is zero. Using these assumptions about the operation of the modulators, and

assuming a 50% duty cycle, the total power dissipated by the device may be written as follows:

$$P_D = \frac{1}{2} [(1-R_{on}) P_{in} + (1 + \frac{\eta q}{h\nu} V_{off}) P_{in}] \quad (15)$$

The prefactor of 1/2 simply reflects the duty cycle. The first term within the brackets is the power dissipated in the on-state, where $V_A=0$ and the power dissipated due to photocurrent is zero. The second term is the power dissipated in the off-state, in which case all of the optical power incident is absorbed, and the applied voltage is $V_A=V_{off}$. This expression can be re-written as follows:

$$P_D = P_{out} * M \quad (16)$$

where

$$P_{out} = R_{on} * P_{in} \quad (17)$$

and

$$M = [\frac{1}{R_{on}} (1 + \frac{1}{2} \frac{\eta q}{h\nu} V_{off}) - \frac{1}{2}] \quad (18)$$

Writing the power dissipation in this way is important for several reasons. First, it relates the power dissipated to the power out. This is important since the power out is a parameter determined by fan-out and detector sensitivity constraints. Given P_{out} , the dissipated power is constant if the parameter M is a constant. M being a constant relates V_{off} to R_{on} linearly. Therefore, by creating a graph of V_{off} vs. R_{on} , contours of constant power dissipation turn out to simply be lines. We have chosen here to plot V_{off} vs. $(1-R_{on})$, which maintains the property of linear power dissipation contours. This is convenient because the insertion loss is equal to $10 \cdot \log_{10} (1-R_{on})$. As described in earlier sections, low modulation voltage and low insertion loss are important characteristics of good modulators. If V_{off} is too high, it will not be compatible with electronic circuit voltages, which are 5V today and headed towards 3.3V. If the insertion loss is too large, P_{in} may need to be too large as calculated by other system considerations, and the device may saturate. For this analysis, I assume a quantum efficiency $\eta=1$ and a operating wavelength of $\lambda_{op}=860\text{nm}$.

The actual graph is shown in Figure IV.11. The abscissa is sub-labeled in terms of insertion loss and R_{on} for convenience. Data points are shown for a number of high contrast modulators published to date. In addition, however, theoretical curves based solely on the quantum well absorption data can be generated for optimum device designs which trade off low voltage for low insertion loss. These turn out to be a function of the front mirror reflectivity, R_f , and so a family of curves can be generated. Figure IV.11 shows curves for the quantum well material used in the UCSB designs at $R_f=0.3$, which corresponds to a device with no front DBR, and $R_f=0.76$, which corresponds to the low voltage, low insertion loss, high contrast device described earlier. The actual devices fall close to the theoretical curves.

The theoretical curves are generated as follows: First, photocurrent measurements are performed on PIN material with no DBR mirrors (i.e. a single pass structure) varying the bias voltage discretely and then sweeping the wavelength. The absorption coefficient for the QW region is extracted from these measurements given the intrinsic region thickness and the well / barrier ratio are known. A family of curves showing absorption as a function of wavelength at a given bias voltage is obtained. For design purposes, these curves may be directly translated into absorption at a given bias electric field simply by dividing the applied voltage by the total width of the intrinsic region of the sample measured. In order to achieve zero reflected power in the off state, equation (2) must be satisfied, which sets the condition:

$$\alpha_{off}l_w = -\frac{1}{2} \ln\left(\frac{R_f}{R_b}\right) \quad (19)$$

where l_w is the total width of the quantum well material (i.e. excluding barriers) in a particular modulator design. This is where the dependence on R_f enters. From the absorption data, one may plot α_{off}/α_{on} where α_{on} refers to the absorption at $E=0$ and α_{off} refers to the absorption at $E=E_{off}$, and so a new family of curves is generated. From this new set of curves, the quantity $\alpha_{on}l_w$ may be determined. Equation (1) may be rewritten and used to find R_{on} for the case of $R_B=1$:

$$R_{on} = \frac{R_f(1-\frac{R_a}{R_f})^2}{(1-R_a)^2} \quad (20)$$

where

$$R_{\alpha} = \sqrt{R_f} \exp(-\alpha_{on} l_w) \quad (21)$$

Clearly, since we wish to minimize the insertion loss, we wish to maximize R_{on} and minimize R_{α} , which means we wish to minimize $\alpha_{on} l_w$ or maximize the ratio α_{off}/α_{on} . At a given field strength, E_{off} , there is a wavelength λ_{op} at which this ratio is a maximum. Substituting the value for $\alpha_{on} l_w$ into equations (21) and (20), we determine R_{on} . Evaluating α_{off} at λ_{op} and knowing $\alpha_{off} l_w$, one can determine l_w . Given the particular quantum well / barrier structure being used, one can then determine the total thickness of the intrinsic region, $l_{MQW} = l_w + l_b$, where l_b is the total barrier thickness. This, combined with the applied electric field yields the applied voltage, $V_{off} = E_{off} * l_{MQW}$. By iterating this calculation at a particular value of R_f over a wide range of E_{off} , one can determine the locus of points of possible modulator designs possible with the quantum well material under consideration. This is what has been done in figure IV.11.

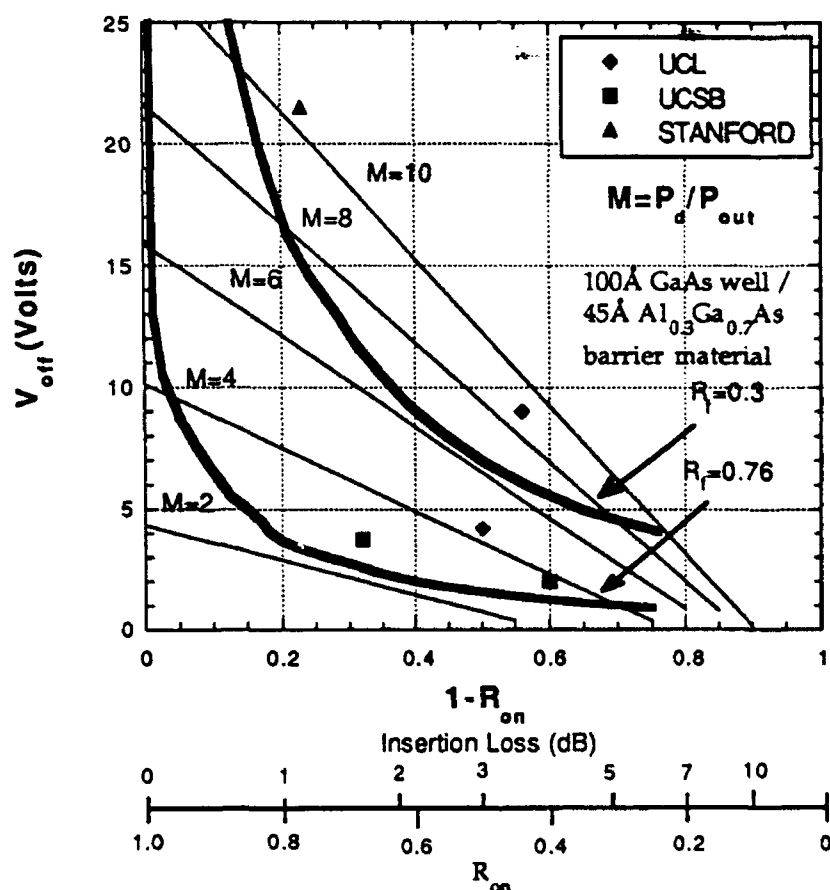
Clearly, the information provided by such a graph is useful because it illustrates the range of possibilities based solely on the quality of the quantum well material which can be grown. As described earlier, the "quality" is a function of such parameters as exciton strength, exciton linewidth, composition of wells and barriers, relative thicknesses of wells and barriers, and growth and processing conditions. As is clear from the data, the UCSB low voltage, low insertion loss, high contrast ratio device is one of the best produced to date.

The general shape of the contours shows that there is a point on a given contour at which the power dissipation will be a minimum. The theoretical curve for the $R_f=0.76$ case has a minimum which is slightly above the $M=2$ line. The UCSB device lies just above this curve at about $M=3$, indicating that it is very close to the optimum design in terms of power consumption as well.

In the preceding analysis, R_f was left as a free parameter. It should be reiterated that the optical bandwidth is a direct function of R_f , and as shown by the equations in figure IV.11, the lower the front mirror power reflectivity, the wider the bandwidth. This was a theme discussed earlier as a primary advantage of asymmetric modulators over symmetric modulators. As can be seen by comparing the two contours for the UCSB

material, one with $R_f=0.3$ and the other with $R_f=0.76$, the performance in terms of power consumption, voltage, and insertion loss has improved, but the optical bandwidth is reduced. In addition, as R_f increases, the thickness of the intrinsic region decreases due to the fact that less absorption is required to reduce the "effective" reflectivity of the back mirror such that it exactly balances the front mirror. This increases the capacitance according to the equations in figure IV.11, and thereby reduces the electrical bandwidth of the device as well.

Lines (Contours) of Constant Power Dissipated ($R_{off} = 0$; $V_{on} = 0$; $R_f = 1$; 50% Duty Cycle)



$$\text{Optical Bandwidth: } \Delta f = \frac{c}{2nL} ; F = \pi \frac{\sqrt{R_f}}{1 - R_f}$$

$$\text{Electrical Bandwidth: } f_c = \frac{1}{2\pi RC} ; C = \frac{\epsilon A}{d}$$

* As the front mirror reflectivity, R_f , increases, the finesse, F , increases and the intrinsic region thickness, d , decreases, thereby reducing both the optical and electrical bandwidth.

Figure IV.11

V. High-Frequency Operation of Fabry-Perot Modulators

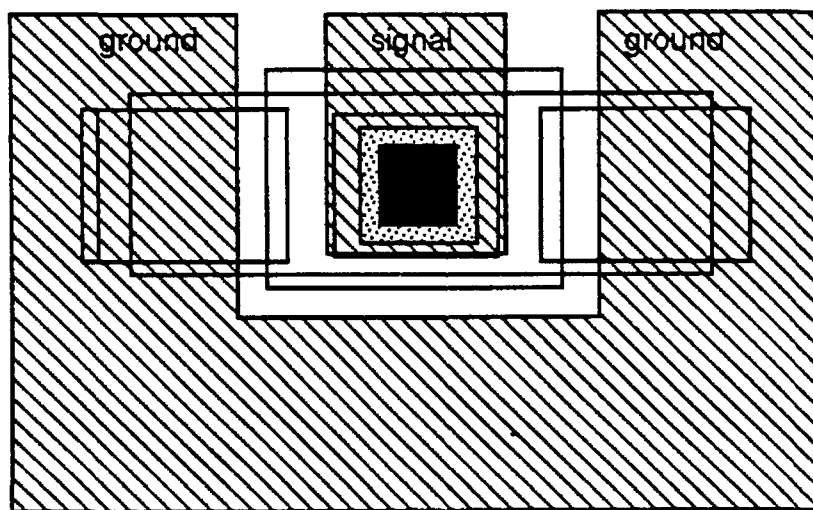
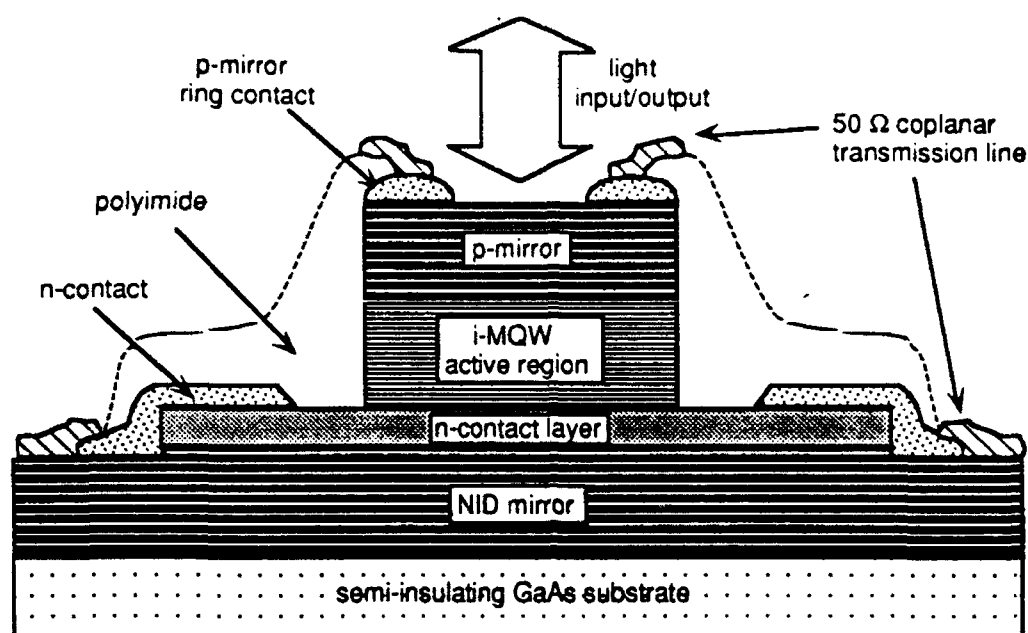
Modulation speed is extremely important for most of the information processing and optical interconnection applications whose promise sparked our interest in Fabry-Perot modulators in the first place. We are currently working towards the fabrication of devices which should run at 30 to 50 GHz.

V.1. Device Structure, Fabrication and Measurement

Our original Fabry-Perot modulator fabrication process consisted simply of evaporating p-contacts onto the MBE-grown material and then cleaving the wafer into reasonably small pieces for testing. Growing the FP étalons on N+ GaAs substrates enabled us to contact the n-doped mirror through the substrate, but the resulting devices were relatively large and slow.

In our first efforts towards achieving high frequency modulators, we were fabricating symmetric Fabry-Perot structures. In order to achieve higher-frequency modulation, we incorporated a highly-doped n-contact layer into the FP cavity to eliminate the series resistance through the substrate and back mirror, developed a two-level mesa fabrication process to delineate smaller, lower capacitance devices, and integrated these smaller devices with 50Ω coplanar microwave probe pads. To further reduce the series resistance, we graded the heterojunctions in the p-mirror. Figure V.1 shows both cross-sectional and top views of a high-speed symmetric FP modulator identical to the one discussed in section II, except for the modifications just mentioned.

The fabrication process we chose to implement first (because of its relative simplicity) consists entirely of "wet" processes and is limited to devices no smaller than about 40μm on a side. The devices we fabricated have dimensions 40μm x 40μm, 60μm x 60μm, and 100μm x 100μm. We measured a 3db electrical bandwidth of 6.5 GHz on SFPMs fabricated using this process.

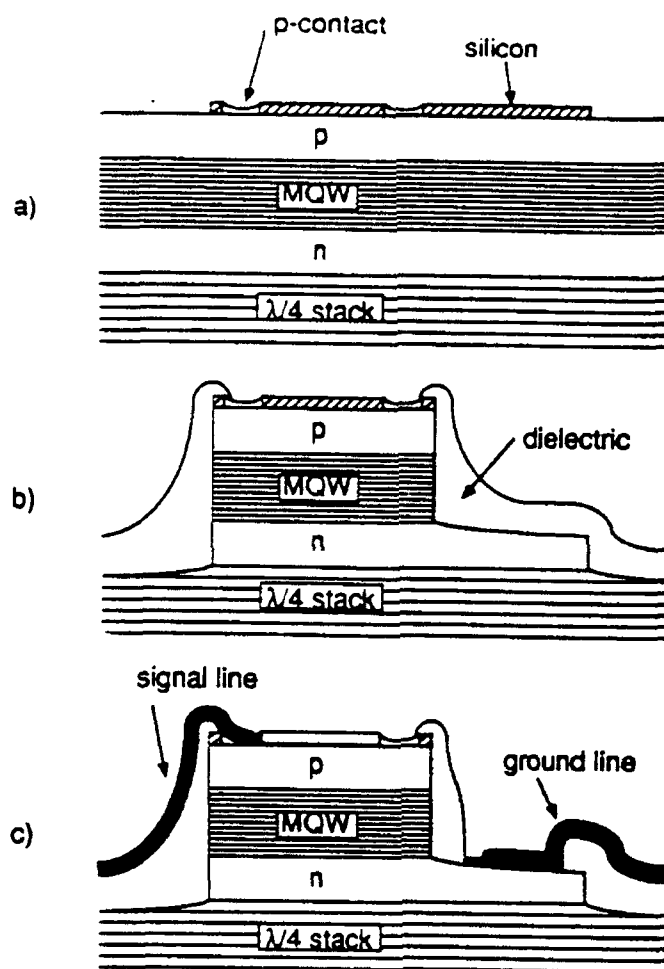


Cross-sectional and top views of a high-speed symmetric Fabry-Perot modulator.

Figure V.1

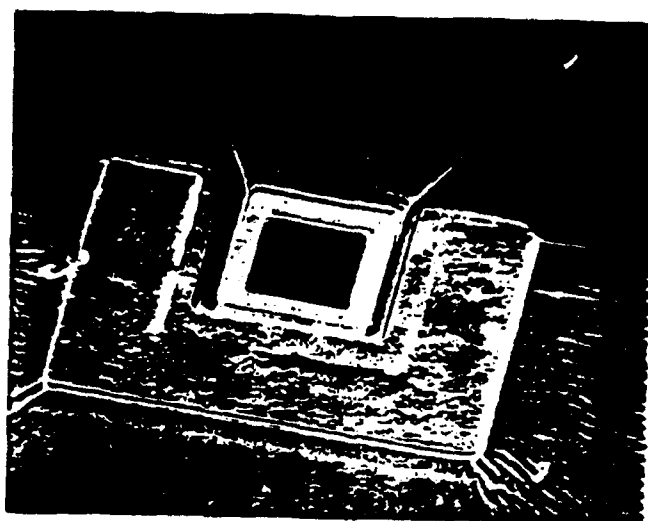
We quickly moved on to asymmetric FPMs, and developed a more sophisticated process which used dry etching techniques to fabricate smaller devices. For the initial demonstration, we chose to use a front mirror power reflectivity of $R_f=0.3$, which corresponds to a simple air-semiconductor interface (i.e. no DBR). This has the clear advantage of eliminating any series resistance caused by transport through the

heterojunctions in a p-mirror. The back mirror had a reflectivity of $R_b=0.99$, the intrinsic MQW region was characterized by 73 100\AA GaAs quantum wells with 100\AA $\text{Al}_{0.2}\text{Ga}_{0.8}\text{As}$ barriers, and $1\mu\text{m}$ thick $\text{Al}_{0.2}\text{Ga}_{0.8}\text{As}$ intracavity contact layers doped to $2 \times 10^{18} \text{ cm}^{-3}$ were used. The device at several stages of processing is shown in Figure V.2. A photograph of finished device is shown in figure V.3.



Modulator Process steps. a) First, areas of silicon are lifted off to protect the surface of the device. The silicon is removed from the p-contact areas with a CF_4 plasma etch and the self-aligned p-contacts are lifted off. b) The n-contact layer is exposed and the devices isolated with a dual-level Cl_2 RIE etch. c) A dielectric layer is applied overall and then removed from the n-contact areas and the tops of the devices. Finally, both n-contacts and probe pads are lifted off.

Figure V.2



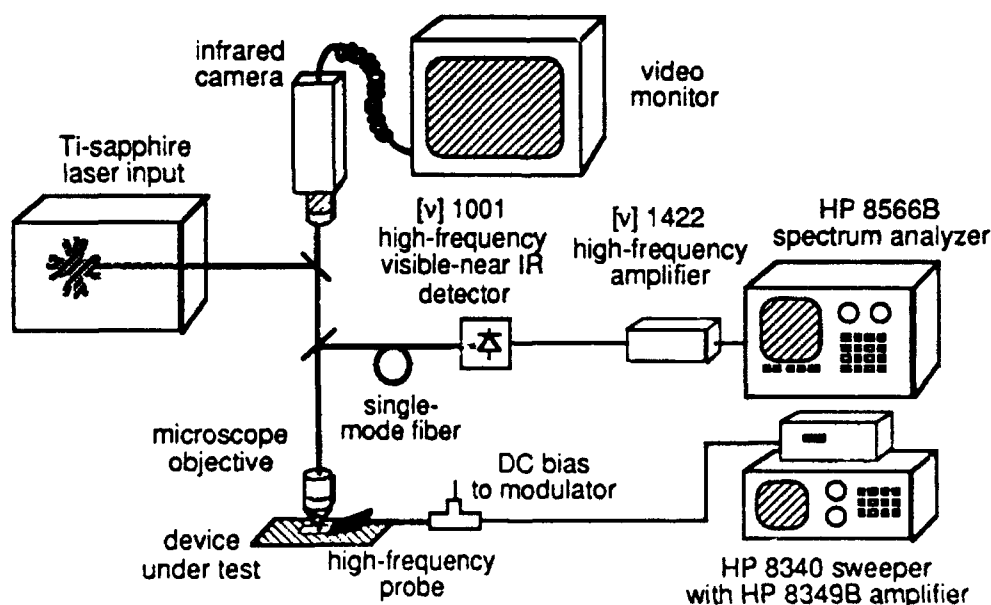
Top view of a completed device.

Figure V.3

The first process step consisted of a simple lift-off of patches of polycrystalline silicon to protect the front mirror surface of the devices from subsequent process steps. Next, we etched through this layer and lifted-off self-aligned Cr:AuZn:Au p-contacts. (For this and all the following lift-offs we employed a dual-layer conformal-mask technology comprising an acetone-soluble planarizing layer of polymethylmethacrylate (PMMA) and a lifted-off nickel mask layer. We undercut the PMMA layer substantially with an oxygen plasma to facilitate the lift-off of thick metal films.) Next we Cl₂ reactive-ion-etched a two-layer mesa structure, masking small squares with nickel and using the silicon areas deposited earlier as a sacrificial mask to retard the etch in the vicinity of each square in order to expose the n-contact layer there. We then spun-on a polyimide dielectric isolation layer, etched it off the tops of the device mesas, and deposited a thin layer of SiO₂ to protect the polyimide from exposure to the oxygen plasmas involved in later process steps. Etching through this dielectric layer, we lifted-off Ni:AuGe:Ni:Au n-contacts, and then defined and lifted-off 50-Ω probe pads of 0.5-μm-thick Ti:Au. Finally, we removed the protective silicon layer from the device windows with a gentle CF₄ plasma etch.

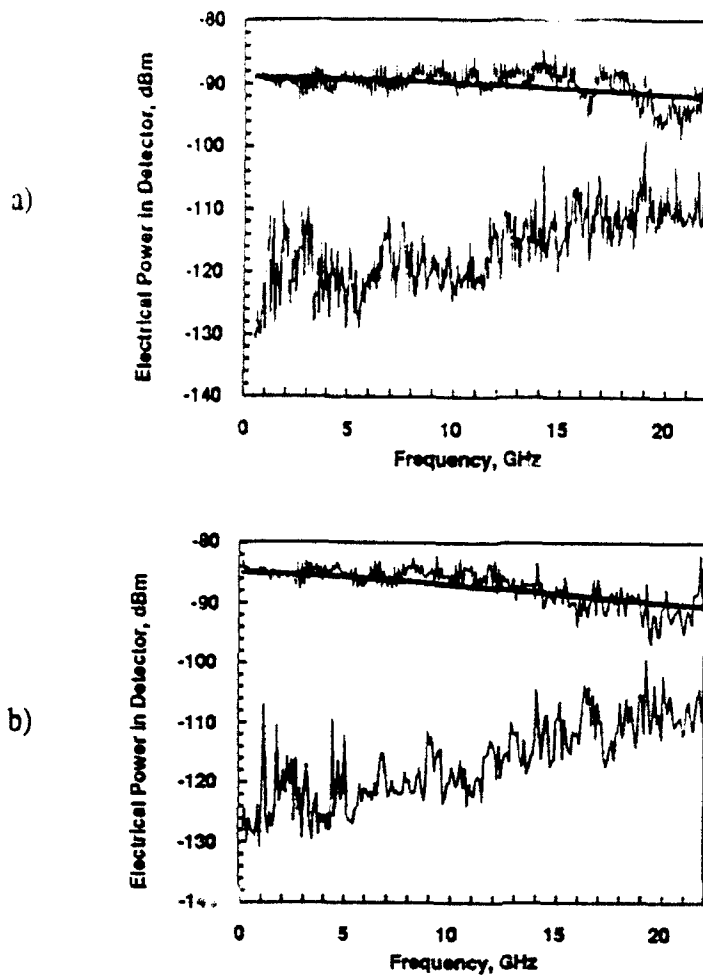
Since the modulator structure we used for these preliminary measurements was not optimized for low-voltage operation, we concentrated on the modulator diodes' relative small-signal performance, using an HP 8340 synthesized sweeper with a Tektronix 40

GHz microwave probe to generate the RF drive voltage and an HP 8566B spectrum analyzer coupled with a high-speed GaAs detector to measure the modulators' response (Fig. V.4). The modulators' performance was optimum at a Ti:Al₂O₃ laser wavelength of 857 nm and a DC bias of 6 to 8 V. We measured the optical response of the modulators for optical powers ranging from about 100 μ W (\sim 300 W/cm²) to 1.5 mW (\sim 4.5 kW/cm² — well into the non-linear regime for these devices [29]). After calibrating the RF sweeper and spectrum analyzer and correcting for the losses in the semi-rigid microwave cabling, bias tees and detector, we estimated the modulators' 3-dB electrical bandwidth to be more than 20 GHz (corresponding to an optical f_{3dB} greater than 34.5 GHz) for the lower-power measurements, and about 15 GHz (optical f_{3dB} = 26 GHz) at the onset of saturation near 500 μ W (Fig. V.5). (Note that the device was not terminated in 50 Ω for these measurements.) A further tripling of the optical input power from 500 μ W to 1.5 mW led to only a 1 dB increase in the modulation level at low frequencies, indicating that the device was severely saturated. Even at this highest optical intensity, however, the 3-dB bandwidth remained about 15 GHz. Instrumentation limitations, as well as the ripple in the data caused by reflections at the microwave probe and interference with radiated signals, prevented a more exact determination of the 3-dB frequencies. Higher-frequency measurements of devices optimized for higher-optical power, lower-voltage operation should yield more precise values.



Configuration of high frequency measurement system.

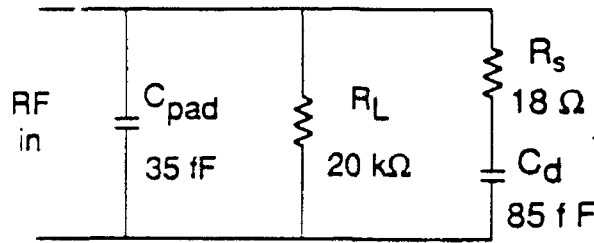
Figure V.4



Two calibrated optical small-signal measurements of the same $30\mu\text{m} \times 30\mu\text{m}$ modulator, showing noise floor and best-fit theoretical curves. Curve a) was taken with $200\mu\text{W}$ of optical power incident on the device and curve b) with $500\mu\text{W}$. We calculated the theoretical curves shown assuming electrical $f_{3\text{dB}}$'s of 21GHz and 15GHz, respectively.

Figure V.5

Figure V.6 shows an electrical circuit model of the modulator diode extracted from S-parameter measurements taken with an HP 8510 network analyzer. The model confirms the reduction in the device capacitance which we achieved by both decreasing the device area and increasing the thickness of the intrinsic region. The series resistance was improved, as expected, by substituting a p-doped AlGaAs contact layer for the front quarter wave stack and reducing the separation between the edge of the n-contact and the device.



Device equivalent circuit extracted from HP 8510 network analyzer measurements to 40GHz.

Figure V.6

Since the RC-limited f_{3dB} this model predicts is

$$f_{3dB} = [2\pi((R_s + Z_0)(\frac{\epsilon A}{I_{MQW}}) + Z_0 C_{pad})]^{-1} \quad (22)$$

we surmise that the device is RC-limited at low optical intensity levels. At high optical power, however, the modulators' speed is clearly limited by some other mechanism, be it the carrier-transport limitations of the MQW active region [15] or an effect of the three-dimensional configuration of the modulator diode [23].

Our speed predictions based upon RC limits alone assume that, because the speed of the quantum-confined Stark effect relies on the rate at which the field switches, and not on the collection rate of the carriers, quantum-well modulators in general will not be limited by transit-time at low optical powers. To test whether our hypothesis still holds for large-signal modulation, we designed a layer structure with a wide intrinsic region which minimizes the device capacitance while maintaining high-contrast, low-voltage-swing operation.

The most efficient material structure for an AFPM employs a high front mirror reflectivity to increase the effective interaction length of the device, shortening the MQW intrinsic region width required to reach the critical absorption, and consequently lowering the voltage. Unfortunately, narrowing the intrinsic region also increases device capacitance, so there emerges a basic trade-off between capacitance (speed) and voltage

swing. By working well off the absorption edge, however, we were able to obtain a sufficient absorption contrast to guarantee large-signal operation with a relatively small electric field change, and thus a reasonable AC voltage swing.

The final material structure, consisting of front and back mirrors with reflectivities of 52% and 99% respectively, a 1- μm MQW operating region composed of 80 100- \AA GaAs quantum wells with 45- \AA $\text{Al}_{0.2}\text{Ga}_{0.8}\text{As}$ barriers, and 0.6- μm -thick $\text{Al}_{0.1}\text{Ga}_{0.9}\text{As}$ intracavity contact layers doped to $2 \times 10^{18} \text{ cm}^{-3}$, was grown by molecular beam epitaxy.

A modification of our previous process was required in order to accommodate an intracavity contact to the p-doped AlGaAs which required etching through the front mirror. The device at several stages of processing is shown in figure V.7. The first process step consists of a simple lift-off of patches of polycrystalline silicon to protect the front mirror surface of the devices from subsequent process steps. Next, we etch through this layer and the front mirror stack and lift-off self-aligned Cr: AuZn: Au p-contacts. (For this and all the following lift-offs we employ a dual-layer conformal-mask technology comprising a soluble planarizing layer of e-beam photoresist (PMGI — Hoechst-Celanese SAL-110-PL1) and a lifted-off nickel mask layer. We undercut the PMGI layer substantially with an oxygen plasma to facilitate the lift-off of thick metal films.) Next we Cl_2 reactive-ion-etch a two-layer mesa structure, masking small squares with nickel and using the silicon areas deposited earlier as a sacrificial mask to retard the etch in the vicinity of each square in order to expose the n-contact layer there. We then sputter-on a dielectric isolation layer of $\approx 0.7 \mu\text{m}$ SiO_2 or SiN_x , and CF_4 -etch it off the tops of the device mesas. Again etching through this dielectric layer, we lift-off Ni: AuGe: Ni: Au n-contacts, and finally define and lift-off 50- Ω probe pads of 0.5- μm -thick sputtered Ti: Au.

We fabricated $16 \mu\text{m} \times 20 \mu\text{m}$ modulators integrated with coplanar microwave probe pads. Figure V.8 shows a photograph of a finished device. Measured wavelength spectra for the finished devices at various bias voltages (Fig. V.9) demonstrate the efficient operation of the modulators at DC. The measured contrast was about 15:1 for a 5 V bias change but in reality the contrast for these modulators is much larger — indeed arbitrarily large at one particular wavelength. In our case much of the measured residual reflection was due to spurious reflections from the periphery of the laser spot, which was a bit too large for the device, rather than reflection from the device window. Simply adding a length of single-mode optical fiber to serve as a spatial filter increased the contrast to 30 dB or more for a 5 V change in bias, while maintaining an insertion loss of 3 dB.

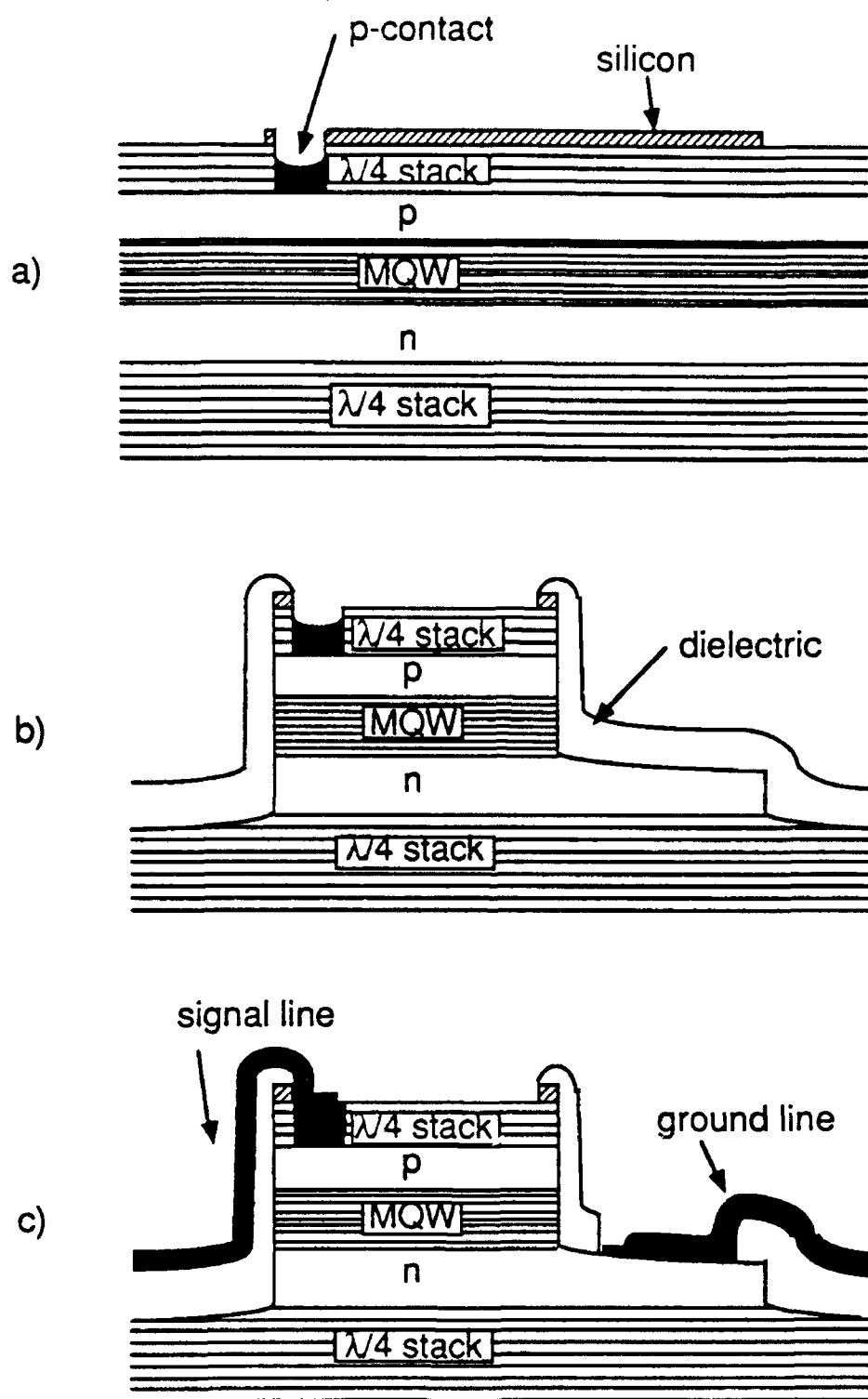
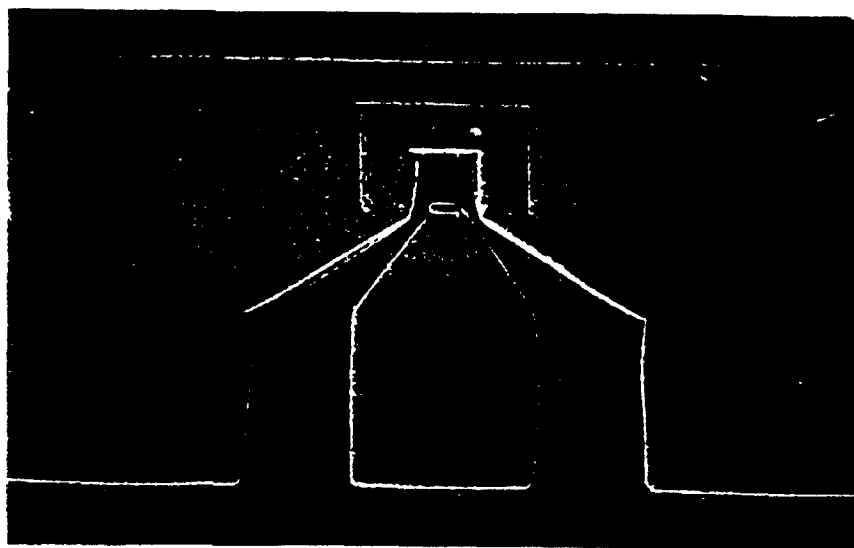
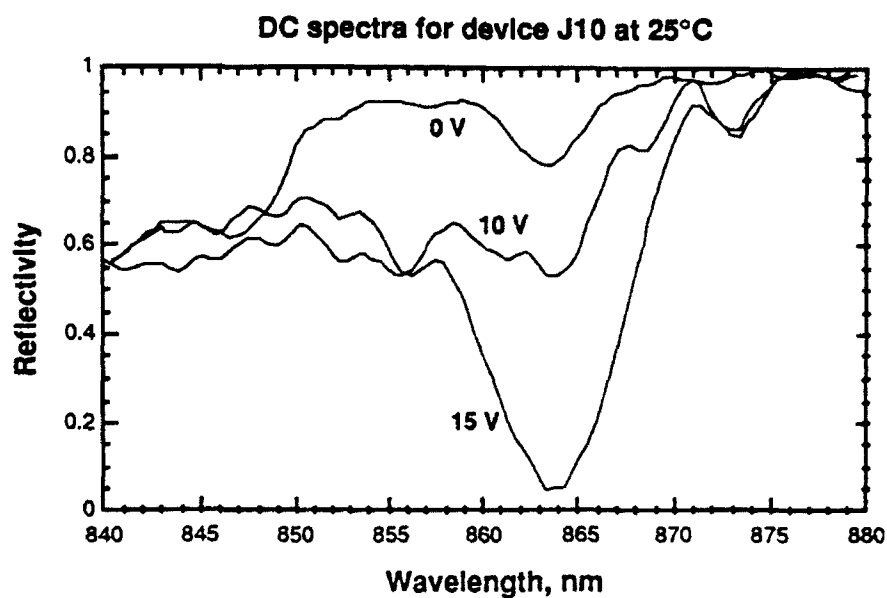


Figure V.7



Scanning electron micrograph of finished $16\mu\text{m} \times 20\mu\text{m}$ device with integrated coplanar microwave probe pad. The optical window is $15\mu\text{m} \times 15\mu\text{m}$.

Figure V.8

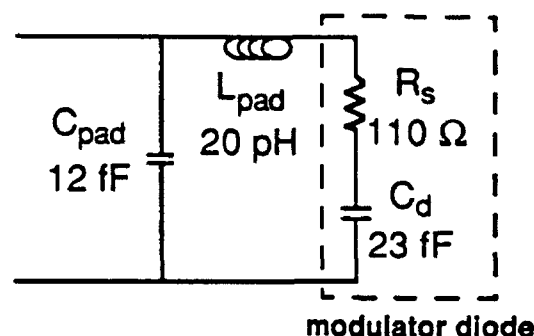


DC spectra of finished $16\mu\text{m} \times 20\mu\text{m}$ device.

Figure V.9

We extracted the device model in Fig. V.10 from network-analyzer measurements of the devices and probe pad patterns. The RC-limited bandwidth predicted from this model is

$$f_{3dB} = \frac{1}{2\pi[C_d(R_s+Z_o)+C_{pad}Z_o]} = 37\text{GHz} \quad (23)$$

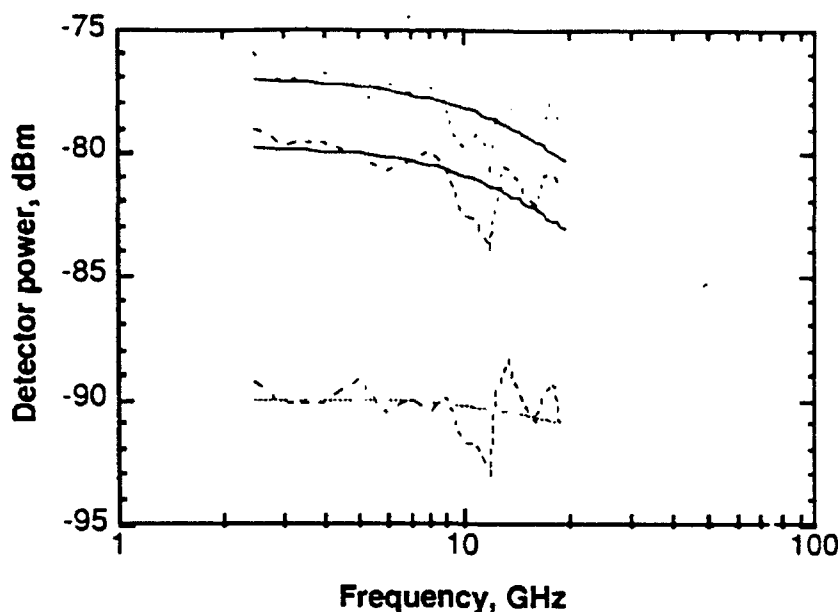


Equivalent circuit for ASFP modulator.

Figure V.10

At optical power levels for which the device is transit-time limited, the bandwidth will be considerably lower, depending on the speed with which the carriers can escape the quantum-well material. Pump-probe measurements suggest that the carrier sweep-out time for comparable quantum-well material and electric fields is about 10 ps, which corresponds to a transit-limited bandwidth of 16 GHz. [5]

We measured the frequency dependence of the AFPM's modulation directly by sweeping the frequency of the microwave drive signal and the spectrum analyzer simultaneously. Subsequently, we measured the roll-off of the various active and passive components and subtracted them from the raw data to obtain the calibrated frequency dependence of the AFPM alone (Fig. V.11). From the curves in Fig. V.11 we see that, just as in our earlier small-signal measurements, the modulators are transit-time limited at the higher optical intensity levels, in this case to a bandwidth of 18 GHz, which corresponds to a transit time of about 9 ps. At lower optical intensities, however, their bandwidth exceeds this transit-time limit, and, indeed, the capabilities of our measurement system.



Swept-frequency modulation measurements at three optical power levels: a) 550 μ W, b) 400 μ W, and c) 80 μ W. Solid lines are theoretical curve fits corresponding to $f_{3dB} = 18$ GHz, 18 GHz, and 37 GHz, respectively.

Figure V.11

For this experiment we applied a 11.5 V DC bias, and a 14 dBm microwave drive signal (corresponding to a 6 V swing). At low optical intensities ($\approx 80 \mu$ W on the device), they switched about 60 μ W at 20 GHz, with 18 dB contrast and 1.5 dB insertion loss. At higher optical intensity levels ($\approx 500 \mu$ W), the AFPMs switched about 350 μ W with >20 dB contrast and 1.5 dB insertion loss at 2-3 GHz. At 18 GHz, the optical modulation was $\approx 125 \mu$ W. With this high-speed performance, AFPMs should find exciting applications in fast "smart pixel" photonic switching and interconnection systems.

V.2. Design Methodology

We will restrict our consideration of the high-speed performance of AFPMs to the situation in which the space charge built up in the quantum wells is insufficient to impact negatively the device performance, either by saturating the exciton or by reducing the effective voltage applied across the MQW region. As discussed above, this amounts to limiting the peak incident optical intensity to relatively low levels (less than, perhaps, 1 kW/cm² or ≈ 0.15 mW on a 10 μ m-diameter device). Subject to this constraint, the device's speed is limited only by the RC time constant associated with the diode

capacitance and series resistance, and the system impedance and parasitic capacitances, and not by any transit-time considerations, as it would be in a photodetector. We can ignore, then, for this analysis, the problems of carrier trapping in and escape from the quantum wells which become important at higher optical powers.[29]

To design a high-speed AFPM, we begin by calculating the absorption-thickness products $(\alpha l_w)_{on}$ and $(\alpha l_w)_{off}$ required in order to give the desired on- and off-state reflectivities (or, equivalently, the desired insertion loss and contrast ratio). The reflectivity at resonance is given by

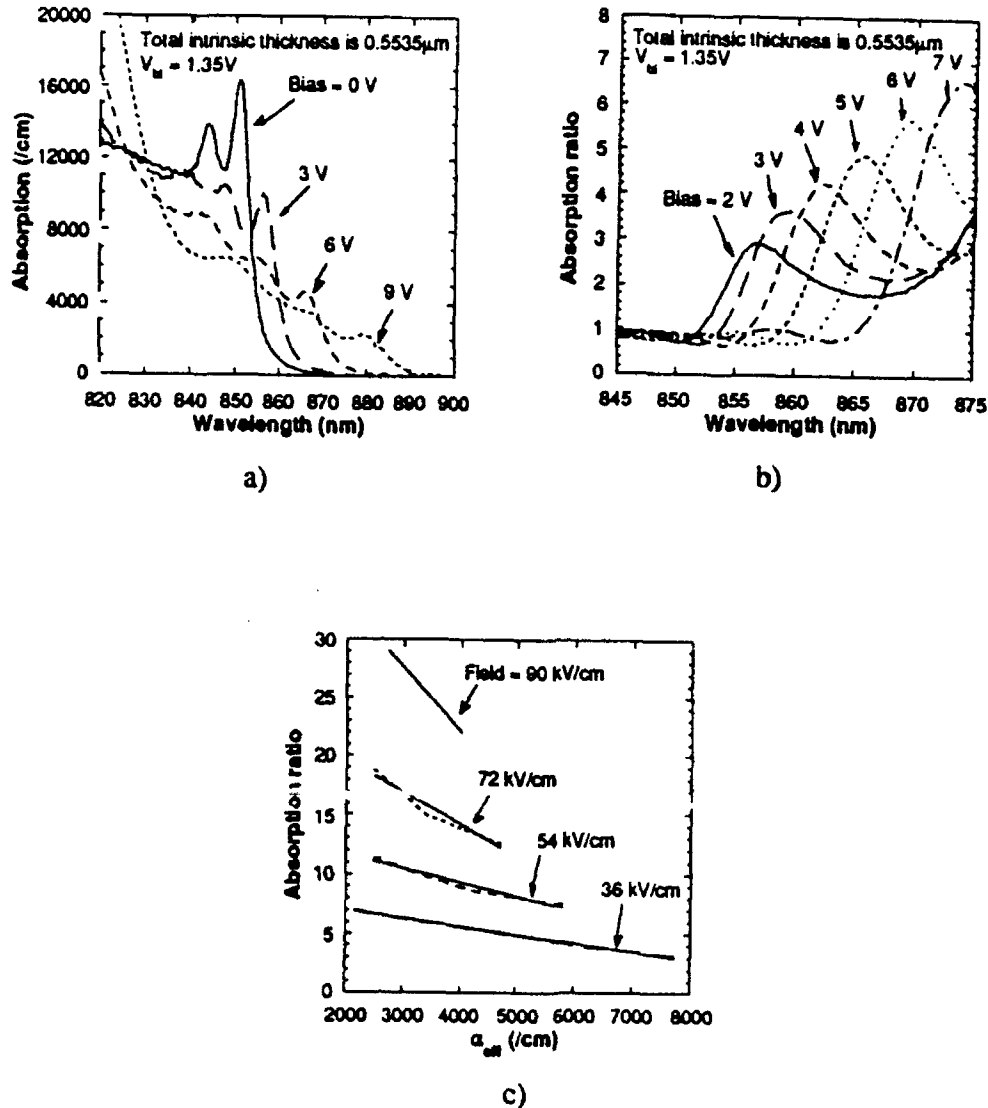
$$R_o = R_f \left(1 - \frac{R_\alpha}{R_f}\right)^2 / (1 - R_\alpha)^2, \quad \text{where } R_\alpha = \sqrt{R_f R_b} \exp(-\alpha l_w) \quad (24)$$

where R_f is the front mirror reflectivity and R_b the back mirror reflectivity. It is useful to consider the ratio of $(\alpha l_w)_{off}$ to $(\alpha l_w)_{on}$, since in general the more demanding the device design parameters, the higher this ratio will have to be. We can derive experimental values of this absorption ratio from measured electroabsorption curves (Fig.V.12). The most efficient designs will then correspond to the peaks in the absorption-ratio curves, or the points of maximum absorption ratio for a given field change ΔE and DC bias. From a plot of this maximum absorption ratio versus the corresponding α_{off} for various values of ΔE we can find the combined thickness of quantum wells l_w , which, for a given ΔE , yields the required $(\alpha l_w)_{off}$ and $(\alpha l_w)_{on}$. The total thickness of the MQW intrinsic region is then $l_{MQW} = l_w + l_b$ (where l_b is the combined thickness of the quantum well barriers), and the operating voltage swing required is $\Delta V = l_{MQW} \Delta E$.

A plot of l_{MQW} versus ΔV (Fig. V.13a) derived from electroabsorption data for a certain MQW structure (e.g. the 100Å GaAs well/ 45Å Al_{0.3}Ga_{0.7}As barrier material of Fig. V.12) constitutes a general design constraint which an AFPM design employing that MQW material must satisfy in order to give the desired contrast and insertion loss. From this curve, then, given the physical structure of the modulator (i.e. its area A, series resistance R_s , and associated pad capacitance C_{pad}), we can plot the predicted electrical bandwidth of the device (Fig. V.13b):

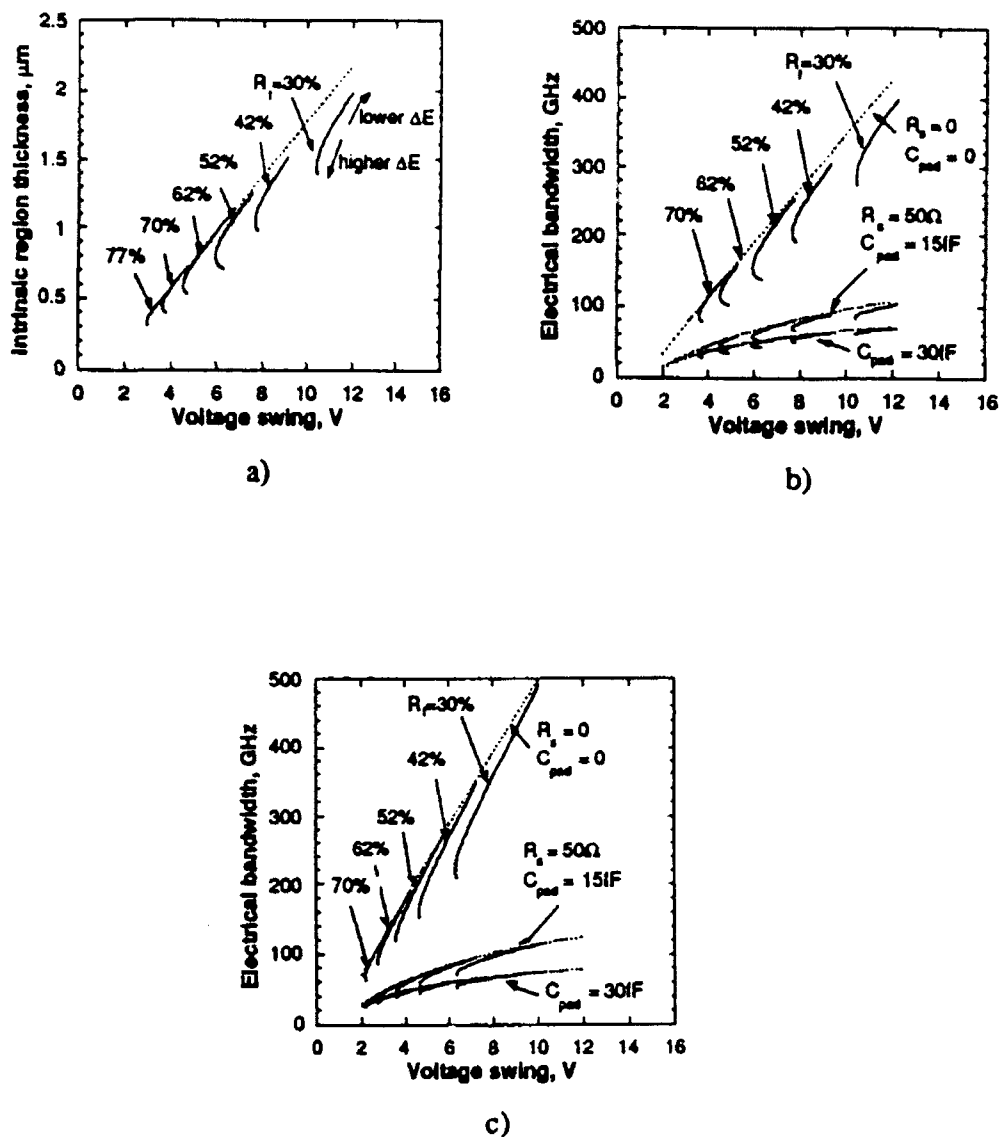
As these plots demonstrate, asymmetric Fabry-Perot modulators do indeed offer high speed, as well as the winning combination of high contrast, low insertion loss, and low operating voltage swings which would be required for high-speed optical switching

arrays. Current devices, such as our recent 21 GHz device[31], are limited by series resistance and pad capacitance; engineering the diode's contacts and the pad design should yield substantial speed improvements for essentially the same modulator structure. Further, design curves such as these facilitate optimizing the material structure itself for high-speed operation.



a) Electroabsorption derived from photocurrent spectroscopy of 100Å GaAs QWs with 45Å $\text{Al}_{0.3}\text{Ga}_{0.7}$ barriers. b) Maximum absorption ratios vs wavelength for 36kV/cm² field change across the structure measured in a) at various biases. c) Maximum absorption ratios and the corresponding values of α_{off} for the same structure. Solid curves are linear fits.

Figure V.12



a) Intrinsic (MQW) layer thickness versus voltage swing for an AFPM layer structure designed to give 20db contrast and 1.5dB insertion loss using the MQW material of figure 12 with various numbers of front quarter-wave stack periods. The solid line shows that the most efficient designs (those for lower ΔE , longer l , and higher bias) fall on a straight line. b) Electrical bandwidth for a $10\mu\text{m} \times 14\mu\text{m}$ diode with the same layer structure as in a), and various values of R_s and C_{pad} . c) Electrical bandwidth for a $10\mu\text{m} \times 14\mu\text{m}$ diode designed to give 15dB contrast with 2db insertion loss. Note that higher speeds can be achieved for the same voltage swing if more insertion loss or lower contrast can be tolerated.

Figure V.13

VI. Circuits and Applications

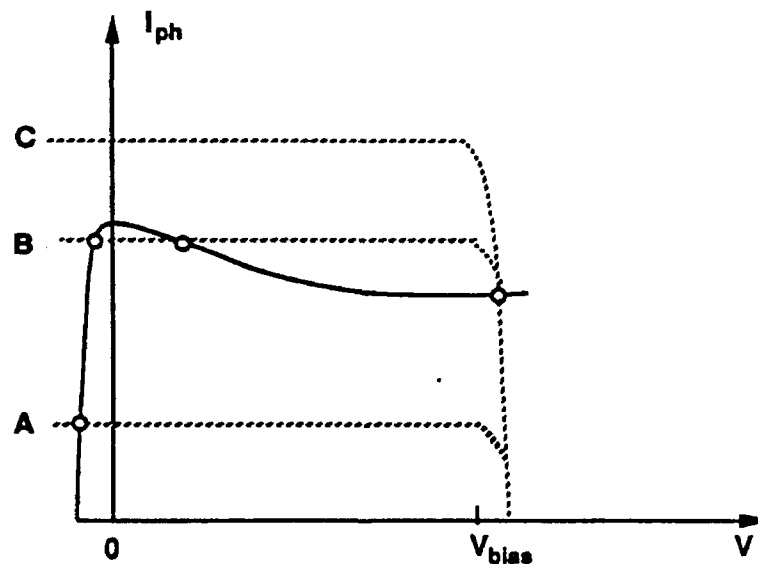
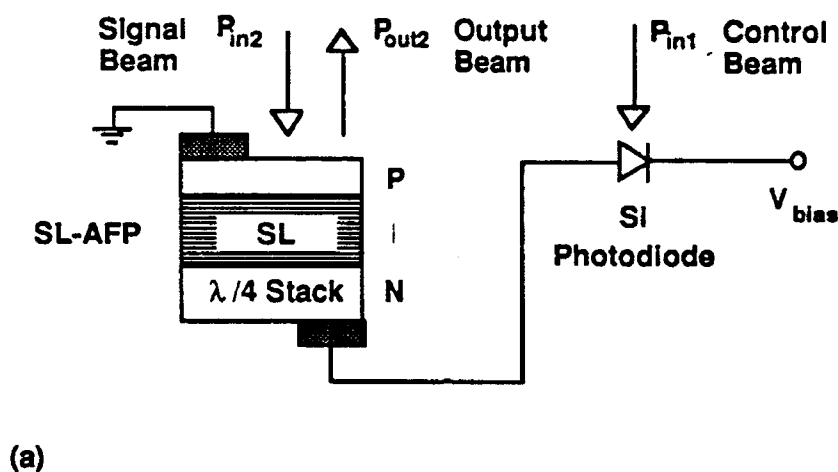
VI.1. Superlattice AFP Bistable SEED

There has been considerable interest in optical switching devices using both semiconductor quantum wells (QWs) and superlattices (SLs). SEEDs are one class of such devices, and are promising elements for future optical information processing systems. The term "SEED" generally applies to any combination of modulator and photodetector which allows the optical output of the device to be set by an optical input. In a quantum well SEED (QW-SEED), a MQW modulator is usually connected in series with a reverse-bias voltage supply and a load element such as a simple resistor. By increasing the incident light intensity at an operating wavelength which coincides with the zero-field QW exciton peak, switching and optical bistability due to positive feedback can be obtained [22]. Also, a more sophisticated load such as a photodiode (or another similar modulator) can be connected in series to form a diode SEED (D-SEED) [33], or a symmetric SEED (S-SEED) [34] to achieve better bistability loop characteristics.

We have exploited the potential of the SL-AFP as a very high-contrast normally-off modulator by connecting the SL-AFP in series with a photodiode and a reverse-biased voltage supply to form a high performance superlattice Fabry-Perot self-electro-optic effect device (SL-FP-SEED) [35].

The SL-FP-SEED configuration is shown in Fig. V.14(a) where the SL-AFP is connected in series with a Si photodiode and a reverse bias voltage supply (≈ 7.5 volts). When both the control beam (power P_{in1}) and signal beam (power P_{in2}) are incident upon the Si photodiode and the SL-AFP respectively, they give rise to photocurrents in the circuit. The current through the Si photodetector must be equal to that through the SL-AFP at steady state, and the voltage across it adjusts itself to ensure this condition is satisfied. The reflected optical output (power P_{out2}) from the SL-AFP is modulated as the voltage across it changes. The operation of this device can be readily understood by considering the photodetector as load for the SL-AFP, as shown in Fig. V.14(b). Here the Si photodetector input intensity is varied and that to the SL-AFP modulator is fixed. The device is bistable whenever there are three intersection points [23], and this will be the case if the SL-AFP is operated at a wavelength where absorption decreases with increasing voltage. Like the S-SEED [34] this device will only be bistable when the

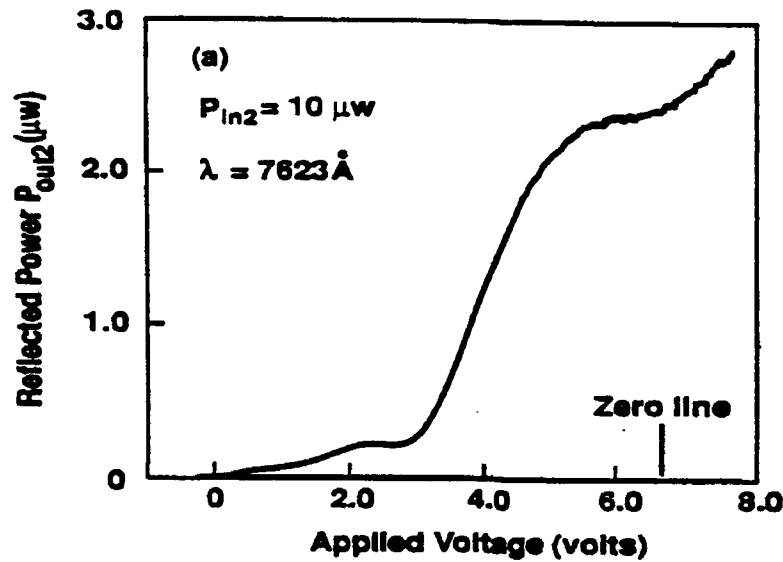
optical input power levels are comparable (line B), and only one single state will exist if the incident power onto the SL-AFP is much higher than that onto the Si photodiode and vice versa (lines A and C respectively).



a) Schematic set-up of the SL-AFP-SEED. P_{in1} and P_{in2} are the incident light power of the Si photodiode and the SL-AFP, respectively. P_{out2} is the reflected output power from the SL-AFP that can be switched by varying P_{in1} . b) Load lines of both the SL-AFP and the Si photodiode. Solid curve is the photocurrent vs voltage for the SL-AFP at one particular input intensity P_{in2} . Dashed lines are the photocurrent vs voltage for the Si photodiode at the three different input intensities P_{in1} . Line B shows that the device is bistable because there are three intersection points between the SL-AFP and the Si photodiode load lines.

Figure V.14

Fig. V.15 shows the reflected power from the SL-AFP as a function of applied voltage at a wavelength $\approx 7620\text{\AA}$. The reflected power reached the zero line when the incident light onto the SL-AFP was blocked. A high contrast ratio of $>100:1$ has been obtained at this wavelength.



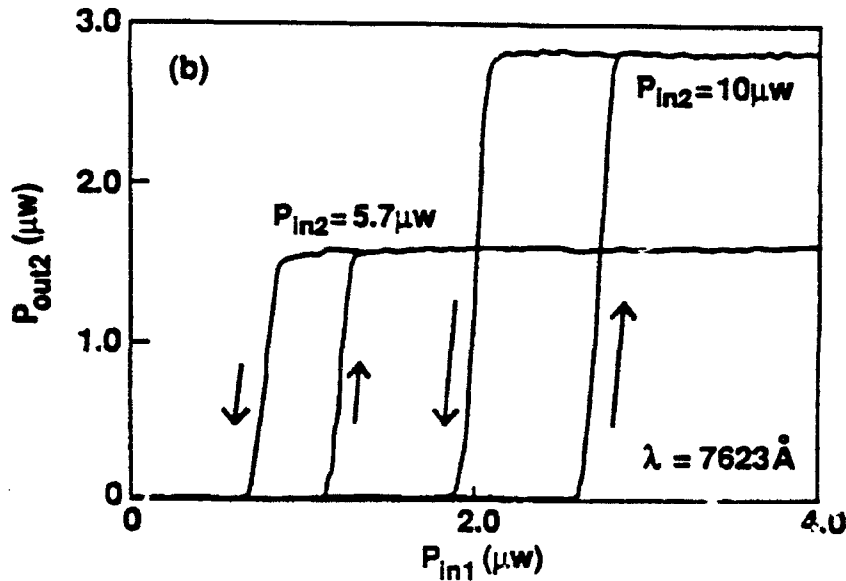
Reflected power of the SL-AFP as a function of voltage at the wavelength 7623\AA . The reflected power reached the zero line when the optical input beam onto the SL-AFP was blocked.

Figure V.15

With the SL-AFP in the SL-FP-SEED configuration (Fig. V.14(a)), we tested for optical bistability by shining light onto the Si photodiode using a commercial GaAs laser diode and illuminating the SL-AFP with the Ti:sapphire laser. The output power of the Ti:sapphire laser was set to be constant for each measurement. The GaAs laser power was ramped up and down to cause the SL-AFP's output to switch state.

Fig. V.16 shows the reflected optical power (P_{out2}) from the SL-AFP as a function of incident intensity (P_{in1}) onto the photodiode for two different signal beam powers (P_{in2}). Optical bistability in the SL-AFP's reflected power with respect to the photodiode's input power could clearly be seen. As shown in Fig. V.16, an on/off ratio of about $130:1$ in the reflected power output was also attained. The output of the device also scaled linearly with the P_{in2} . Likewise, the device's bistability loop width also varied proportionally

with P_{in2} , as expected [22]. Optical bistability could be observed in a wide spectral range and an on/off ratio of more than 10:1 was obtained over an optical bandwidth of $\approx 30\text{\AA}$.



Output power (P_{out2}) reflected from the SL-FP-SEED vs control power (P_{in1}) for different signal powers (P_{in2}). An on/off ratio in P_{out2} of 130:1 was attained.

Figure V.16

The potential advantage of incorporating SL-AFP into SEEDs can be further extended by connecting two such modulators in series with a reverse-bias voltage supply to form a high performance S-SEED. The external bias voltage of such an S-SEED can also be reduced or eliminated by employing SL-AFPs with lower operating voltage, obtained by properly reducing the active region thickness and increasing the top mirror reflectivity.

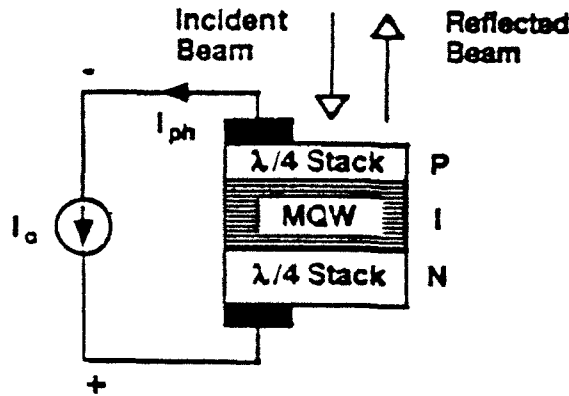
VI.2. Superlattice AFP Linearized SEED

For analog signal processing applications, it is advantageous that the optical output depend linearly on the control input, be it electrical or optical. It is well known that the modulated optical output with respect to the drive voltage of neither a simple QW non-Fabry-Perot modulator nor an ASFP is linear. To improve the linearity of the optical output signal of the modulator with respect to the input control signal, we operate a QW-AFP with simultaneously very low insertion loss, high contrast and low drive voltage as a

SEED, where current biasing of the AFP is used. The optical modulation of the AFP is expected to vary linearly with drive current and exhibit similar high performance with low switching energy.

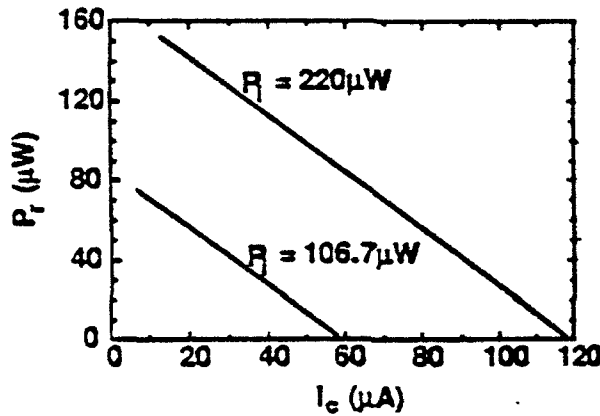
The AFP device structure contains top and bottom quarter-wave stacks respectively of 5 periods p-doped and 20.5 periods n-doped alternating 725\AA AlAs and 625\AA $\text{Al}_{0.2}\text{Ga}_{0.8}\text{As}$ layers. The active region inside the Fabry-Perot cavity is composed of 25.5 pairs 100\AA GaAs QWs confined by 45\AA AlAs-GaAs SPSLs. In contrast to that of the optically bistable SEED, the internal optoelectronic feedback in the present case is negative because the operating photon energy is at the FP mode of the normally-on AFP where the photocurrent increases with increasing reverse-bias voltage, due to increasing absorption caused by the red shift of the QW exciton. As shown in Fig. V.17, a voltage-control current source is connected to the AFP in reverse bias. When the current I_C from the current source is larger (smaller) than the photocurrent I_{ph} generated by the AFP, then it will charge up (discharge) due to the current difference. This in turn adjusts the voltage across the AFP to yield increased (decreased) absorption and hence increases (decreases) I_{ph} until the stable equilibrium point $I_C = I_{ph}$ is reached. At this point, if the internal quantum efficiency of the AFP is unity, then the absorbed optical power P_A is given by $h\nu I_C/q$, where $h\nu$ is the photon energy and q is the electronic charge. Since P_A is linearly dependent on the control current I_C , the reflected power P_r given by $P_r = P_i - P_A$ (very good approximation because the transmitted power of such AFP is very small compared with P_i and P_A) is therefore a linearly decreasing function of I_C . Further, P_A can be expressed as AP_i where A is the fraction of light absorbed in the active cavity and is a function of the active medium absorption coefficient and the FP cavity parameters. At the FP resonance, A is virtually complementary to the FP reflectivity, and this can lead to the virtual extinction of the reflected power of the balanced AFP with sufficient drive current.

Shown in Fig. V.18 are the output powers versus drive current curves for two different optical input powers at the FP wavelength (866nm). Except in the low current region close to $I_C \approx 0\mu\text{A}$ where the reflected power is limited by the AFP's insertion loss ($<1.6\text{db}$), the AFP's reflected power decreases linearly with increasing current to a minimum given by its 'zero' reflectivity, yielding contrast ratio of $>100:1$ at the output. In the linear region, the rate of change of P_r with respect to that of I_C is given by the fundamental parameters $h\nu/q$, as evidenced by the slopes of the curves in Fig. V.18.



Schematic diagram of the SEED consisting of a current source connected to reverse bias the normally-on ASFP.

Figure V.17



Reflected output power as a function of the drive current at the FP wavelength for two different input optical powers.

Figure V.18

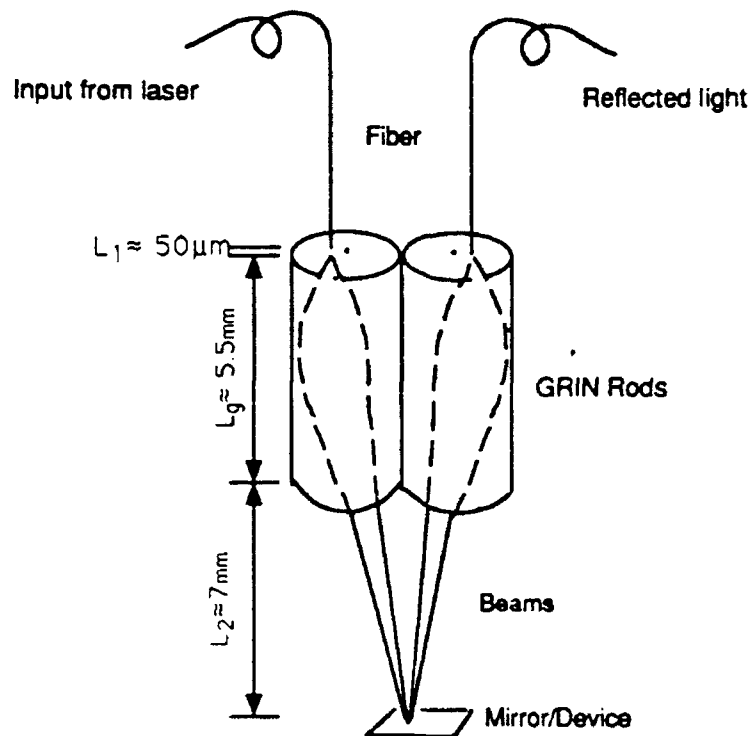
The speed of the current device operation is dependent on the speed of charging and discharging the AFP P-I(QW)-N diode by the I_c and I_{ph} difference. The current demonstrated SEED can also be in other configurations where the AFP is integrated with electronic components to extend the device versatility and increase potential applications.

VI.3. Fiber-to-Fiber Coupling Interface for Transverse Modulators

Prior to employing transverse modulators in systems, one must examine methods of efficiently coupling light into and out of these modulators. We have been pursuing a low loss fiber interconnect system that is also low in cost, as well as being portable.

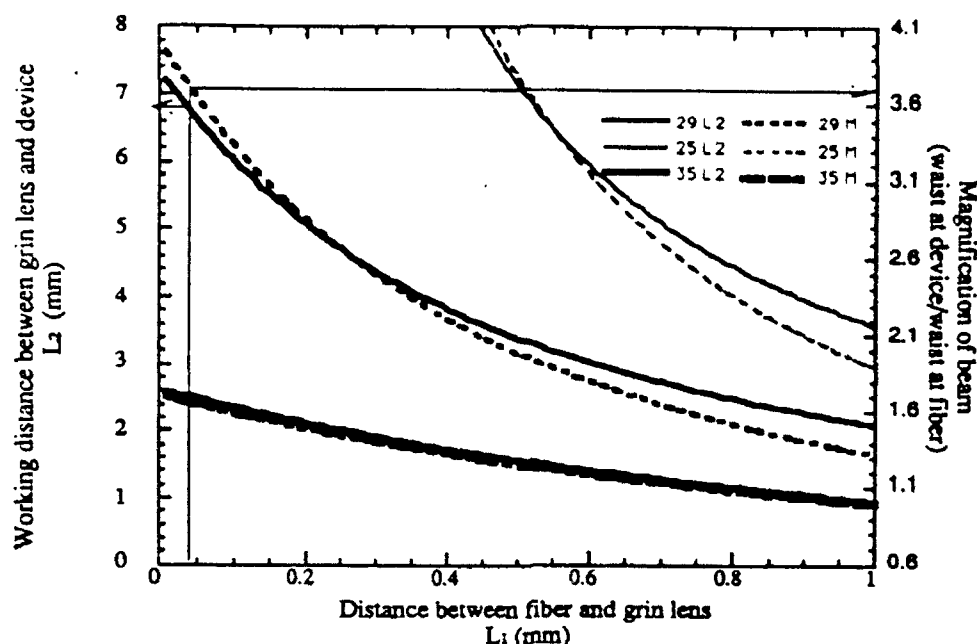
Shown in Fig V.19. is the coupling scheme that has been designed to meet these goals. The coupling involves two GRIN rods (graded index lens) 1.8mm in diameter and 5.5mm long (L_g). Light in a GRIN rod propagates sinusoidally which results in focusing characteristics dependent on L_g . The GRIN lens can be modeled as a normal lens with a working distance (L_2) and a magnification that varies as a function of fiber to GRIN distance (L_1). These curves are plotted for three values of pitch (pitch μL_g) in Fig. V.20. We used a pitch of 0.29 because it is commercially available and we desired a longer working distance (7mm). The magnification is not presently an issue (a 60 μ m device was used) but future systems using smaller, high speed devices may require a larger pitch GRIN rod.

With the fibers positioned slightly off center, a focus point half way between the GRIN centers can be achieved (see Fig. V.19). If both of the fiber/GRINs are focusing to this same point then, with a mirror at this point, the light should efficiently couple from one fiber to the other. For the 0.29 pitch GRIN, the angle of incidence on the device was 7 degrees, well within the operating range of the Fabry Perot. Our novel approach of utilizing GRIN lenses for this purpose has led to some promising results.



Coupling scheme for a fiber to ASFP modulator.

Figure V.19



Grin lens to device (L_2) and magnification (M) as a function of fiber to GRIN (L_1) for three different pitches 0.25, 0.29, 0.35.

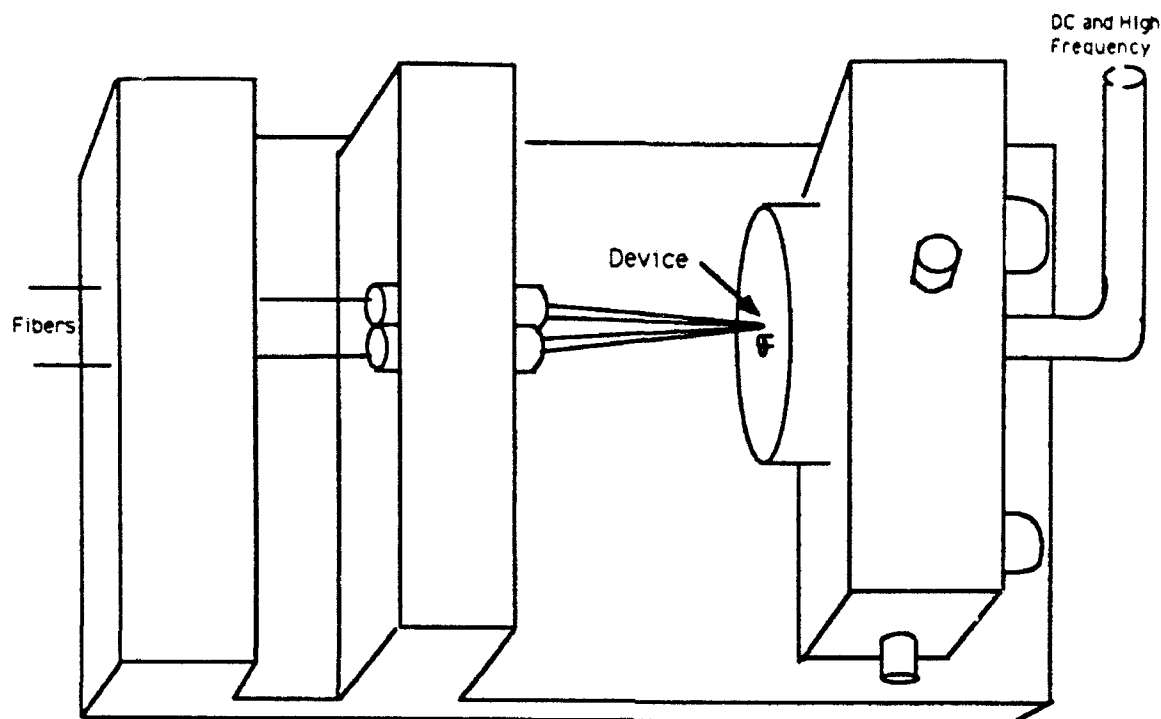
Figure V.20

Alignment consists of independent xyz control (for each fiber) and xyz + rotation control for the device. Once alignment was achieved and the fibers were epoxied into place, then the xyz controls on the fibers were removed. The final package would include the 5 axis mount for the device, a high frequency (with DC bias) input, and a input and output for the fibers (Fig. V.21).

The beam waist at the modulator (Fig. V.22) was approximately $25\mu\text{m}$, as expected, since the beam waist out the fiber is $6.4\mu\text{m}$ and the magnification is approximately 3.7X. The variation in coupling efficiency versus length L_2 and device angle, was less than 1 dB over $50\mu\text{m}$ and 0.3 degrees, respectively. The coupling efficiency varied less than 0.5 dB over the wavelength range of 840-900nm.

The loss in the fibers that were used (fiber connector plus end reflection) was 0.3 dB. The coupling loss of the total system (fibers, GRIN rods, and a 100% mirror) was 3.3 dB without any epoxy between the fibers and the GRINs, and 1.8 dB with un-cured UV epoxy. At 865nm, this particular device is highly reflective, which resulted in a total on state loss of 2 dB. While at the designed operating point of 859nm, the on state was -6.5 dB and the off state -31.8 dB. This contrast ratio of 25 dB was similar to that obtained

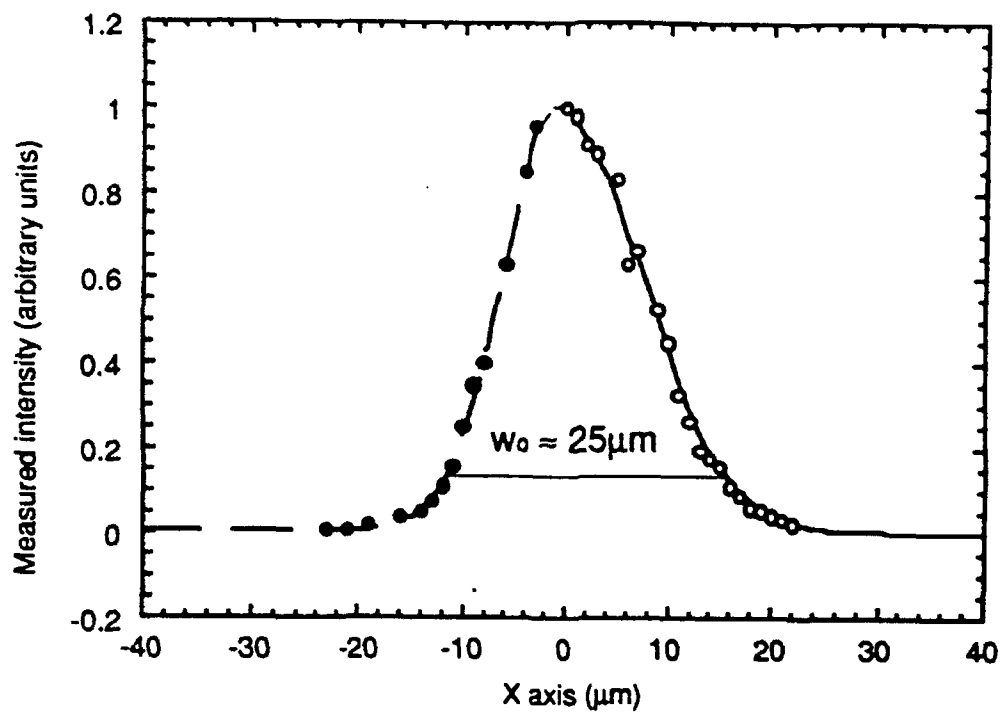
via our bulk optics measurements and the on state was only 2 dB lower. These results show that using an AFPM and two GRIN rods with off axis fibers is a viable way to achieve high contrast, low insertion loss, fiber coupled modulation.



Final package includes: 5 axis mount for the device, high frequency (with DC bias) electrical input, and fiber input and output.

Figure V.21

When the epoxy was cured, there was an additional 1 dB of loss due to a submicron shift in the fiber's position. The previous epoxies used did not cure 100% and as a result, the fiber alignment was lost over a period of days. In the future, we will be using an epoxy with a high viscosity and a 100% cure. Once long term durability is obtained, the package can be used as a high speed, portable, fiber coupled modulator.



Measured beam waist at the device (along the x axis) via a $5 \mu\text{m}$ aperture.

Figure V.22

References

- [1] T. H. Wood, "Multiple quantum well (MQW) waveguide modulators", J. Lightwave Tech. 6, 743 (1988).
- [2] R. H. Yan, R. J. Simes, L. A. Coldren, and A. C. Gossard, "Transverse modulators with a record reflection change of $> 20\%$ /V using asymmetric Fabry-Perot structures", Appl. Phys. Lett. 56, 1626 (1990).
- [3] T. Y. Hsu, W. Y. Wu, and U. Efron, "Amplitude and phase modulation in a 4- μm -thick GaAs/AlGaAs multiple quantum well modulator", Electron. Lett. 24, 603 (1988).
- [4] G. D. Boyd, D. A. B. Miller, D. S. Chemla, S. L. McCall, A. C. Gossard, and J. H. English, "Multiple quantum well reflection modulator", Appl. Phys. Lett. 50, 1119 (1987).
- [5] R. B. Bailey, R. Sahai, and C. Lastufka, "1x16 arrays of GaAs/AlGaAs multiple quantum well optical modulators with 26:1 contrast", Optical Society of America, Topical Meeting on Quantum Wells for Optics and Optoelectronics, 1989, Paper PD-1 (Salt Lake City, Utah, 1989).
- [6] R.J. Simes, R.H. Yan, R. S. Geels, L. A. Coldren, J. H. English, A. C. Gossard, and D. G. Lishan, "Electrically tunable Fabry-Perot mirror using multiple quantum well index modulation", Appl. Phys. Lett. 53, 637 (1988).
- [7] Y. H. Lee, J. L. Jewell, S. J. Walker, C. Tu, J. P. Harbison, and L. T. Florez, "Electro-dispersive multiple-quantum-well modulator", Appl. Phys. Lett. 53, 1684 (1988).
- [8] R. H. Yan, R. J. Simes, and L. A. Coldren, "Electroabsorptive Fabry-Perot reflection modulator using asymmetric mirrors", IEEE Photon. Tech. Lett. 1, 273 (1989).
- [9] R. H. Yan, R. J. Simes, and L. A. Coldren, "Analysis and design of surface-normal Fabry-Perot electro-optic modulators", IEEE J. Quantum Electron. 25, 2272 (1989).

- [10] D. A. B. Miller, D. S. Chemla and S. Schmitt-Rink, "Electric field dependence of optical properties of semiconductor quantum wells", in *Optical Nonlinearities and Instabilities in Semiconductors*, H. Haug, ed., Academic, New York, 1988. (and the references therein).
- [11] M. Whitehead and G. Parry, "Low-voltage multiple quantum well reflection modulator with on:off ratio > 100:1", *Electron. Lett.* 25, 984-5 (1989).
- [12] R. H. Yan, R. J. Simes, and L. A. Coldren, "Extremely low-voltage surface-normal reflection modulators", *IEEE Photon. Tech. Lett.* 2, 118 (1990).
- [13] R. H. Yan, K-K Law, L. A. Coldren, and J. L. Merz, "Asymmetric Fabry-Perot reflection modulator using red- and blue- shifted electro-absorption effects", *J. Appl. Phys.*, 68, (2), 875-877, (1990).
- [14] R. S. Geels, S. W. Corzine, J. W. Scott, D. B. Young, and L. A. Coldren, "Low threshold planarized vertical-cavity surface-emitting lasers", *IEEE Phot. Tech. Lett.* 2, 234 (1990).
- [15] R. H. Yan, R. J. Simes, and L. A. Coldren, "Wide-bandwidth, high-efficiency reflection modulators using an unbalanced Fabry-Perot structure", *Appl. Phys. Lett.* 55, 1946 (1989).
- [16] K. Fujiwara and K. Ploog, "Photoluminescence of GaAs single quantum wells confined by short-period all-binary GaAs/AlAs superlattices", *Appl. Phys. Lett.*, 1984, 45, pp. 1222-1224, and the references therein.
- [17] R. H. Yan, R. J. Simes, and L. A. Coldren, "Extremely low-voltage Fabry-Perot reflection modulators," *IEEE Photon. Tech. Lett.*, 1990, vol. 2, pp. 118-119.
- [18] K-K Law, M. Whitehead, J. L. Merz, L. A. Coldren, "Simultaneous achievement of low insertion loss, high contrast, and low operating voltage in asymmetric Fabry-Perot reflection modulator," *Electronics Lett.*, 27, 1863 (1991).

- [19] R.H. Yan, R.J. Simes, H. Ribot, L.A. Coldren and A.C. Gossard, "Blue-Shifted Absorption using Field-Induced Stark Localization in Superlattices," CLEO '89, MJ4, Baltimore, MD, (April 1989).
- [20] J. Bleuse, G. Bastard and P. Voisin, Phys. Rev. Lett. 60, 220 (1988); J. Bleuse, P. Voisin, M. Allovon and M. Quillec, Appl. Phys. Lett. 53, 2632 (1988); E. E. Mendez, F. Agullo-Rueda and J. M. Hong, Phys. Rev. Lett., 60, 2426 (1988).
- [21] K-K. Law, R.H. Yan, J.L. Merz, and L.A. Coldren, "Normally-Off High-Contrast Asymmetric Fabry-Perot Reflection Modulators Using Wannier-Stark Localization in Superlattices," Applied Physics Lett., 56, 1886, (May 7, 1990).
- [22] D. A. B. Miller, D. S. Chemla, T. C. Damen, T. H. Wood, C. A. Burrus, Jr., A. C. Gossard and W. Wiegmann, "The quantum well self-electro-optic effect device: Optoelectronic bistability and oscillation, and self-linearized modulation", IEEE J. Quantum Electron., QE-21, 1462 (1985).
- [23] R. H. Yan and L. A. Coldren, "Effect of temperature on the operating characteristics of asymmetric Fabry-Perot reflection modulators", Appl. Phys. Lett., 57, (3), 267-269, (1990).
- [24] D. I. Babic and S. W. Corzine, J. Quantum Electron., 28, 514, (February 1992).
- [25] J.-P. Weber, K. Malloy, and S. Wang, IEEE Photon. Tech. Lett., 2, p. 162, 1990.
- [26] K-K. Law and D. I. Babic, private communication.
- [27] S. Schmitt-Rink, D.S. Chemla and D.A.B. Miller, Phys. Rev. B, 32, pp.6601-6609 (1985).
- [28] T.H. Wood, J.Z. Pastalan, C.A. Burrus Jr., B.C. Johnson, B.I. Miller, J. L. deMiguel, U. Koren, and M.G. Young, Appl. Phys. Lett., 57, p.1081 (1990).
- [29] A. M. Fox, D. A. B. Miller, G. Livescu, J. E. Cunningham, J. E. Henry, and W. Y. Jan, "Exciton saturation in electrically biased quantum wells," Appl. Phys. Lett., vol. 57, pp. 2315-2317, 1990.

- [30] R.A. Morgan, L.M.F. Chirovsky, M.W. Focht and R.E. Leibenguth, Appl. Phys. Lett., 59, p.3524, (1991).
- [31] C.C. Barron, M. Whitehead, K.-K. Law, J.W. Scott, M.E. Heimbuch, and L.A. Coldren, "K-band operation of asymmetric Fabry-Perot modulators," IEEE Photonics Technology Letters (to appear May, 1992).
- [32] R.S. Geels and L.A. Coldren, "Low Threshold, High Power, Vertical-Cavity Surface-Emitting Lasers," Electron. Lett., 27, (21) 1984-1985, (October 10, 1991).
- [33] D. A. B. Miller, J. E. Henry, A. C. Gossard and J. H. English, "Integrated quantum well self-electro-optic effect device: 2x2 array of optically bistable devices", Appl. Phys. Lett, 49, 821 (1986).
- [34] A. L. Lentine, H. S. Hinton, D. A. B. Miller, J. E. Henry, J. E. Cunningham And L. M. F. Chirovsky, "Symmetric self-electro-optic effect device: Optical set-reset latch", Appl. Phys. Lett, 53, 1419 (1988).
- [35] K-K. Law, R.H. Yan, L.A. Coldren, and J.L. Merz, "A Self-electro-optic device based on a superlattice asymmetric Fabry-Perot modulator with an on/off ratio >100:1," Applied Physics. Lett., 57, (13), 1345-1347, (September 24, 1990).

VII. Conference and Journal Publications

Previously Reported Publications (9/30/89 - 3/31/92)

- [1] "Blue-Shifted Absorption using Field-Induced Stark Localization in Superlattices,"
R.H. Yan, R.J. Simes, H. Ribot, L.A. Coldren and A.C. Gossard,
CLEO '89, MJ4, Baltimore, MD, (April 1989).
- [2] "Electro-Absorptive Fabry-Perot Reflection Modulators with Asymmetric Mirrors,"
R.H. Yan, R.J. Simes, and L.A. Coldren,
IEEE Photonics Technol. Lett., 1, (9) 273-275, (September 1989).
- [3] "Multiple Quantum Well Asymmetric Fabry-Perot Reflection Modulators,"
R.H. Yan, R.J. Simes and L.A. Coldren,
IEEE LEOS '89, OE3.2, Orlando, FL, (October 1989).
- [4] "Analysis and Design of Surface-Normal Fabry-Perot Electro-Optic Modulators,"
R.H. Yan, R.J. Simes, and L.A. Coldren,
IEEE J. Quantum Electron., 25, pp. 2272-2280, (November 1989).
- [5] "Wide-Bandwidth, High-Efficiency Reflection Modulators Using an Unbalanced Fabry-Perot Structure,"
R.H. Yan, R.J. Simes, and L.A. Coldren,
Applied Physics Lett., 55, (19), 1946-1948, (November 6, 1989).
- [6] "Extremely Low-Voltage Fabry-Perot Reflection Modulators",
R.H. Yan, R.J. Simes, L.A. Coldren,
IEEE Photonics Technol. Lett., 2, (2), (February 1990).
- [7] "Transverse Modulators with a Record Reflection Change of $>20\%/V$ Using Asymmetric Fabry-Perot Structures,"
R.H. Yan, R.J. Simes, L.A. Coldren, and A.C. Gossard,
Applied Physics Lett., 56, (17), 1626-1628 (April 23, 1990).

- [8] "Normally-Off High-Contrast Asymmetric Fabry-Perot Reflection Modulators Using Wannier-Stark Localization in Superlattices,"
K-K. Law, R.H. Yan, J.L. Merz, and L.A. Coldren,
Applied Physics Lett., 56, 1886, (May 7, 1990).
- [9] "Superlattice Asymmetric Fabry-Perot Reflection Modulator,"
K-K. Law, R.H. Yan, L.A. Coldren and J.L. Merz,
CLEO'90, paper no. CTUC3, Anaheim, CA, (May, 1990).
- [10] "A Self-Electro-Optic Effect Device Using Superlattice Asymmetric Fabry-Perot Modulators",
K-K. Law, R.H. Yan, L.A. Coldren and J.L. Merz,
1990 Device Research Conference, paper VIB-4, Santa Barbara, CA,
(June 1990).
- [11] "Surface-Normal Electro-Absorption Reflection Modulators Using Asymmetric Fabry-Perot Structures,"
R.H. Yan, R.J. Simes, and L.A. Coldren,
IEEE J. Quantum Electron., (To be published July 91).
- [12] "Asymmetric Fabry-Perot Reflection Modulators Using Red- and Blue-Shifted Electroabsorption Effects,"
R.H. Yan, K.K. Law, L.A. Coldren, and J.L. Merz,
J. Applied Physics, 68, (2), 875-877, (July 15, 1990).
- [13] "Effect of Temperature on the Operating Characteristic of Asymmetric Fabry-Perot Reflection Modulators,"
R.H. Yan and L.A. Coldren,
Applied Physics Lett., 57, (3), 267-269, (July 16, 1990).
- [14] "Self-Electro-Optic Effect Device Based on an Asymmetric Fabry-Perot Modulator Using Wannier-Stark Localization in Superlattice,"
K.K. Law, R.H. Yan, L.A. Coldren, and J.L. Merz,
NLO (Nonlinear Optics) '90, Kauai, Hawaii, paper no. TP15, (July 16 - 20, 1990).

- [15] "A Self-electro-optic device based on a superlattice asymmetric Fabry-Perot modulator with an on/off ratio >100:1,"
K-K. Law, R.H. Yan, L.A. Coldren, and J.L. Merz,
Applied Physics. Lett., 57, (13), 1345-1347, (September 24, 1990).
- [16] "High-Frequency electro-optic Fabry-Perot Modulator,"
R.J. Simes, R.H. Yan, C.C. Barron, D. Derickson, D.G. Lishan, J. Karin,
L.A. Coldren and M. Rodwell,
IEEE Photonics Technol. Lett., (To be published June 1991).
- [17] "High-Efficiency Vertical-Cavity Surface-Emitting Lasers and Modulators,"
(INVITED PAPER)
L.A. Coldren,
SPIE'90, 1362, Aachen, Germany, (October 28 - November 2, 1990),
- [18] "High Performance Fabry-Perot Transverse Optical Modulators," (INVITED PAPER)
L.A. Coldren and R.H. Yan,
LEOS'90, Boston, MA, paper no. OE7.1, (November 4-9, 1990).
- [19] "Optical modulation and switching using GaAs/AlGaAs Superlattice Asymmetric Fabry-Perot Modulator grown by MBE,"
K-K. Law, R.H. Yan, J.L. Merz and L.A. Coldren,
European MRS'90, Strasbourg, France, Paper no. A-12.5, (November 27-30, 1990).
- [20] "Measurement of field-induced refractive index variation in a GaAs/AlGaAs superlattice using a monolithic Fabry-Perot etalon,"
K-K. Law, R.H. Yan, L.A. Coldren and J.L. Merz,
Electronics Letters, 27, No.2, pp. 105-106 (Jan 17 1991)
- [21] "High-contrast Fabry-Perot Electroabsorption Modulators," (INVITED PAPER)
R-H. Yan, R.J. Simes, and L.A. Coldren,
Quantum Optoelectronics Topical Meeting, paper no. MB1-1, Salt Lake City, UT, (March 11-13, 1991).

- [22] "Large excitonic blue-shift and nonlinearity in narrow asymmetric coupled quantum wells,"
Y.J. Ding, C.L. Guo, S. Li, J.B. Khurgin, K-K. Law, J. Stellato, C.T. Law, A.E. Kaplan and L.A. Coldren,
Quantum Optoelectronics Topical Meeting, Paper no. MD6-1, Salt Lake City, UT, (March 11-13, 1991).
- [23] "Low-Voltage Superlattice Asymmetric Fabry-Perot Reflection Modulator,"
K-K. Law, L.A. Coldren, and J.L. Merz,
IEEE Photonics Tech. Letts., 3, (4) 324-326, (April, 1991).
- [24] "Very Low-Voltage MBE-grown Asymmetric Fabry-Perot Reflection Modulator based on Superlattice Wannier-Stark Localization,"
K-K. Law, J.L. Merz, and L.A. Coldren,
APCT'91 Clearwater, FL, paper no. 227, 210-213, (May 1991).
- [25] "Observation of Anomalously Large Excitonic Blue-Shift and Optical Bistability in Narrow Asymmetric Coupled Quantum Wells,"
Y.J. Ding, C.L. Guo, S. Li, J.B. Khurgin, K-K. Law, J. Stellato, C.T. Law, A.E. Kaplan and L.A. Coldren,
CLEO'91, Baltimore, MD, paper no. CMB5, (May 12-17, 1991).
- [26] "High-Frequency electro-optic Fabry-Perot Modulator,"
R.J. Simes, R.H. Yan, C.C. Barron, D. Derickson, D.G. Lishan, J. Karin, L.A. Coldren and M. Rodwell,
Photonics Tech. Lett., 3, (6) 513-515, (June 6, 1991).
- [27] "Simultaneous Achievement of Low Insertion Loss, High Contrast and Low Operating Voltage in Asymmetric Fabry-Perot Reflection Modulator,"
K-K. Law, M. Whitehead, J.L. Merz, and L.A. Coldren,
Electron. Lett., 27, (20), 1863- 1865, (September 26, 1991).
- [28] "K-Band Operation of Asymmetric Fabry-Perot Modulators,"
C.C. Barron, M. Whitehead, K.-K. Law, J.W. Scott, M.E. Heimbuch and L.A. Coldren,
IEEE LEOS'91, San Jose, CA, paper no. PD8, (November 4-7, 1991).

Recent Publications (4/1/92 - 3/31/93)

- [29] "K-band operation of asymmetric Fabry-Perot modulators,"
C. C. Barron, M. Whitehead, K-K. Law, J. W. Scott, M. Heimbuch, and
L. A. Coldren,
IEEE Photon. Lett. 4, p. 2051-2053 (Apr., 1992).

- [30] "High-contrast self-linearized optical modulation of a SEED based on a normally-on asymmetric Fabry-Perot modulator with record combined characteristics,"
K-K. Law, L. A. Coldren, and J. L. Merz,
LEOS'92 Summer Topical Meeting of Broadband Analog and Digital
Optoelectronics, Santa Barbara, CA, Paper ThC3, (July 29-31, 1992).

- [31] "Effect of layer thickness variations on the performance of asymmetric Fabry-Perot reflection modulators,"
K-K. Law, J. L. Merz, and L. A. Coldren,
J. Appl. Phys., 72, p. 855-860 (Aug., 1992).

- [32] "High-speed design of asymmetric Fabry-Perot modulators,"
C. C. Barron, M. Whitehead, K-K. Law, and L. A. Coldren,
IEEE Leos Summer Topical Meeting on Smart Pixels, Santa Barbara, CA,
paper WB2 (Aug. 10-12, 1992).

- [33] "Superlattice surface-normal asymmetric Fabry-Perot reflection modulators:
optical modulation and switching,"
K-K. Law, J. L. Merz, and L. A. Coldren,
to be published in J. Quantum Electron.

- [34] "Self-linearized optical modulation of a normally-on asymmetric Fabry-Perot
modulator with high contrast, low insertion loss, and low operating energy",
K-K. Law, J. L. Merz, and L. A. Coldren,
submitted to Jpn. J. Appl. Phys..

VIII. Personnel

1. Prof. Larry A. Coldren, Principal Investigator
2. Prof. Arthur C. Gossard, Co-Principal Investigator
3. Carole C. Barron, PhD student
4. Geoff Thompson, PhD student
5. Mark Whitehead, visiting Research Engineer
6. Cathal Mahon, visiting Research Engineer